Marine and Petroleum Geology 170 (2024) 107161

Contents lists available at ScienceDirect

Marine and Petroleum Geology

journal homepage: www.elsevier.com/locate/marpetgeo

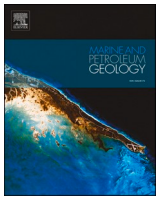

Coupled evolution of basin structure and fluids recorded by microfractures: A case study of deep-buried ordovician in the tarim basin

Jian Wang [a,b,c,*], Dongping Tan [a,b], Yingchang Cao [a,b,c,**], Jun Han [d], Haijun Yang [e], Yin Liu [a,b], Keyu Liu [a,b,c]

[a] State Key Laboratory of Deep Oil & Gas, China University of Petroleum (East China), Qingdao 266580, China
[b] School of Geosciences, China University of Petroleum (East China), Qingdao, 266580, China
[c] Laboratory for Marine Mineral Resources, Qingdao Marine Science and Technology Center, Qingdao, 266071, China
[d] Northwest Oil Field of China Petrochemical Group, Urumqi, 830011, China
[e] PetroChina Tarim Oilfield Company, Korla, 841000, China

ARTICLE INFO

Keywords:
Microfracture
Diagenetic fluid evolution
Carbonate rock
Strike-slip fault
Ordovician
Tarim basin

ABSTRACT

The fluid activity in the deep strata of sedimentary basins is commonly related to tectonic activity, and the cements filled in fractures are a good carrier for the tectonic-fluid coupling evolution. Compared to macro-fractures, microfractures have characteristics of high frequency and easy identifiable periods. Abundant microfractures infilled by carbonate cements (MCCFs) developed in carbonates of the Ordovician Yingshan and Yijianfang formations in the platform basin area of the Tarim Basin. Based on the study of petrology, U-Pb dating, and geochemical characteristics, this study determined the stages of MCCFs and clarified the tectonic-fluid coupling evolution process recorded by MCCFs in the study area. The formation order of these MCCFs is D1, C1, C2, D2, C3, and C4. The precipitation times of MCCFs have a good correspondence with orogeny around the Tarim Basin and active times of strike-slip faults in the platform basin area. The six stages of MCCFs in the Ordovician Yingshan and Yijianfang formations in the SLU recorded the tectonic-fluid coupling evolution process of concentrated seawater in the late Middle Ordovician, meteoric water at late Ordovician, organic acids during the Silurian, Mg-rich hot brine at the end Devonian-early Carboniferous, and magmatic hydrothermal fluids during the Permian. This not only indicates a close connection between fluid activity and tectonic activity in sedimentary basins, but also confirms that the formation of MCCFs in carbonate formations is closely related to regional tectonic-fluid coupling activities. This study provides a good example for studying macro scale tectonic-fluid coupling activities in basins using microfractures.

1. Introduction

Fluid activity is the most active geological agent in hydrocarbon-bearing basins (Leythaeuser and Krooss, 1996; Parnell, 2010). Fluid-rock interactions widely exist in all geological processes of basin evolution (Leythaeuser and Krooss, 1996), controlling the evolution and distribution of materials and energy, especially closely related to diagenesis, reservoir evolution, and oil and gas accumulation processes in sedimentary basins (Lander et al., 2008; Olson et al., 2009; Wang et al., 2016, 2018, 2021, 2022). Fluid activity in sedimentary basins is commonly related to tectonic movements, especially in deep buried strata where fluid activity is usually driven by tectonic activity (Kareem et al., 2019; Wang et al., 2022). Fractures are one of the important channels for fluid migration, material and energy exchange in tight carbonate or clastic rocks (Philippe and Manuel, 1998; Uysal et al., 2000; Marfil et al., 2005; Morad et al., 2010; Cooley et al., 2011). Carbonate cements filled in fractures (CCFs) are extremely common in carbonate formations and are one of the direct products of fluid-rock interaction (Caja et al., 2003, 2006; Morad et al., 2010). CCFs can record information on the composition of diagenetic fluids (Rossi et al., 2001; Wang et al., 2023a), temperature and pressure conditions (Eichhubl and Boles, 2000; Becker et al., 2010; Worden et al., 2016), diagenetic fluid environment and fluid sources (Worden et al., 2016; Yang et al., 2022a,b; Wang et al., 2023a) during their precipitation

* Corresponding author. State Key Laboratory of Deep Oil & Gas, China University of Petroleum (East China), Qingdao 266580, China.
** Corresponding author. State Key Laboratory of Deep Oil & Gas, China University of Petroleum (East China), Qingdao, 266580, China.
E-mail addresses: wangjian8601@upc.edu.cn (J. Wang), caoych@upc.edu.cn (Y. Cao).

https://doi.org/10.1016/j.marpetgeo.2024.107161
Received 12 May 2024; Received in revised form 13 October 2024; Accepted 15 October 2024
Available online 18 October 2024

process. Meanwhile, CCFs are also a good carrier for studying the history of fault activity (Roberts and Holdsworth, 2022). They can be used to reveal fluid activity in low-temperature (<300 °C) sedimentary basins (Dockrill and Shipton, 2010; Bons et al., 2012), indicate the pattern of geological fluid movement (Worden et al., 2016), and infer the impact of tectonic movements on fluid activity (Jin et al., 2008; Wang et al., 2022, 2024). Isotope chronology analysis of CCFs can constrain basin deformation, fault activity stages and time (Suchy et al., 2000; Nothdurft et al., 2004; Barker et al., 2009; Nuriel et al., 2012; Guo et al., 2016; Roberts et al., 2017; Roberts and Holdsworth, 2022; Yang et al., 2022a, b).

The quality of small fractures is usually more than large ones in many fracture populations (Ortega et al., 2006; Barbier et al., 2012; Hooker et al., 2012; Watkins et al., 2020). Microfractures with straight traces and small aspect ratios are usually corresponding with macrofractures in subsurface rocks (Laubach and Gale, 2006). These types of microfractures and their associated macrofractures belong to the same set of fractures and have the same origin (Gomez and Laubach, 2006; Laubach and Gale, 2006). Therefore, microfractures can help determine information about the development of macrofractures and reveal some issues related to fractures that are difficult to explore (Marrett et al., 1999; Ortega et al., 2006; Hooker et al., 2009). Due to its good recognizability and accessibility, fractures at core scale are currently commonly used data for studying tectonic or fluid activities in basins (Suchy et al., 2000; Curtis, 2002; Barker et al., 2009; Nuriel et al., 2012; Gasparrini et al., 2014; Yang et al., 2022a,b; Wang et al., 2023). However, due to the influence of core size, fractures at the core scale usually cannot fully display the sequential relationship between fractures of different periods, leading to significant limitations in using them to study tectonic activity or fluid evolution (Laubach and Gale, 2006). Microfractures that develop simultaneously with core scale fractures not only have consistent origins, but also can present a relatively complete sequence of fracture development stages (Gomez and Laubach, 2006; Laubach and Gale, 2006). During the filling process of fractures, microfractures with small openings are the first to fill, followed by fractures with large openings (Laubach, 2003; Hooker et al., 2012). Moreover, compared to macrofractures, microfractures usually to be infilled completely with no or little fracture porosity preserved (Ukar and Laubach, 2016), which can effectively preserve the fluid information during filling process. Therefore, when using fractures to study structure or fluid evolution, microfractures have advantages that macrofractures do not possess. At present, study on micro fractures in carbonate reservoirs mainly focuses on the genesis, characterization, controlling factors of fracture development, the impact of fractures on reservoir properties and permeability, and the corresponding fluid during microfractures sealing (Zeng and Li, 2009; Anders et al., 2014; Ougier-Simonin et al., 2016; Ezati et al., 2018; Wang et al., 2023). However, there are few reports on the use of microfractures to study the tectonic-fluid coupling evolution.

Several large-scale strike-slip faults developed in the SLU of the platform basin area of the Tarim Basin (Wu et al., 2021). Controlled by regional tectonic movements, the strike-slip fault in the study area has undergone multiple periods of activity. As a result, a complex multi-scale fracture system has developed in the Yingshan and Yijianfang formations (Wu et al., 2018, 2020 ab). Strike-slip faults and multi-scale fracture systems are advantageous channels for communicating formation fluids, and play a crucial role in the formation of carbonate reservoirs (Lu et al., 2017; Baqués et al., 2020; Ding et al., 2020; Wu et al., 2020b; Zhao et al., 2020; Wang et al., 2022, 2024). Fluid activity formed widely distributed CCFs in the Yingshan and Yijianfang formations, with particularly developed microscale CCFs (MCCFs) at the thin section scale. In the study, we determine the stages, precipitation time, and geochemical characteristics of MCCFs based on systematic analysis of petrology, and explore the relationship between the precipitation sequence of MCCFs and the tectonic-fluid coupling evolution process. This can not only clarify the tectonic-fluid evolution process experienced by the Ordovician in the Tarim Basin, provide a fluid basis for the study of fault-controlled reservoirs, but also provide a good example for the study of basin tectonic-fluid coupling activities using MCCFs.

2. Geological background

Located in the south of Xinjiang Uygur Autonomous Region (Fig. 1A), the Tarim Basin is a hydrocarbon-bearing basin located in the Tarim plate, with an area of about 56×10^4 km^2 (Wang et al., 2024). Tarim Basin is located in the transitional zone between the Ural and Tethys orogenic belts (Ma et al., 2013; Zhang et al., 2013; Liu et al., 2016a,b), with Tianshan Mountains in the north, Kunlun Mountains in the south, and Altyn Mountains in the southeast (Fig. 1B). Tarim Basin is a typical superimposed basin, which has experienced multiple periods of intense tectonic movements.

SLU is located in the northern slope belt of the central Tarim Basin, with the Manjiaer Depression in the east, the Awati Depression in the west, the Shaya Uplift in the north and the Katake Uplift in the south (Fig. 1C and D). The SLU experienced stable tectonic subsidence under the weak extensional background in the early Caledonian period, the formation of low uplifts under the regional compression background in the middle and late Caledonian to early Hercynian periods, the transformation from the late Hercynian to Indosinian periods (Wang et al., 2020a), and the fault activation and finalization stages from the Yanshanian to Himalayan periods (Han et al., 2017; Wang et al., 2020a). Corresponding to various tectonic activities, multiple strike-slip faults developed in the SLU (Fig. 1C and D). In recent years, a number of light oil or condensate reservoirs were found in the ultra-deep marine carbonate rocks in the SLU of the platform basin area in the Tarim Basin (Lu et al., 2017; Han et al., 2019; Ding et al., 2020; Wang et al., 2022). Unlike the unconformity karst reservoirs represented by Tahe and Tazhong oil fields, the reservoirs in the Yingshan and Yijianfang formations of the SLU are mainly fault-controlled ultra-deep fractured and vuggy reservoirs formed under the control of intra-cratonic strike-slip faults (Lu et al., 2017; Han et al., 2019; Ding et al., 2020; Wang et al., 2024). The strike-slip fault activity has formed multiple periods and scales of fractures with carbonate cements infilled in the Yingshan and Yijianfang formations (Fig. 2).

In the early Caledonian period, a set of hydrocarbon source rocks of slope facies developed in the Shuntuoguole area during the early Cambrian. During the early-middle Ordovician, a set of platform facies carbonate rocks, including the Yingshan and Yijianfang formations, developed in the study area (Figs. 1D and 2A). In the mid Caledonian period, NE and NW strike-slip faults developed in the SLU, and the late Ordovician carbonate platform was submerged (Figs. 1D and 2). The Shuntuoguole area evolved into a mixed shelf, depositing thick mudstones and forming high-quality regional cap rocks (Tang et al., 2014). In the late Caledonian to early Hercynian period, the SLU was continuously compressed, and the strike-slip fault developed in succession, penetrating the Cambrian downwards and connecting the source rocks at the bottom of the Cambrian (Yang et al., 2022a,b). In the middle and late period of the Hercynian period, the SLU continued to rise, and a large amount of igneous rocks developed in the middle Permian (Ma et al., 2013). During the Indosinian-Yanshanian period, the Shuntuoguole area continued to be deeply buried. During the Himalayan period, the SLU underwent adjustment and shaping, with the activation of strike-slip faults, forming the current pattern (Liu et al., 2016a,b; Wu et al., 2020a).

3. Materials and methods

Seismic section data was collected from the Northwest Oilfield Company SINOPEC. The high-resolution seismic data had a frequency of 30–40 Hz. The SEG standard was used, and the black and red reflectors had positive and negative polarities, respectively. Thirty-seven core samples were collected from 19 wells in the study area (Fig. 1C). All

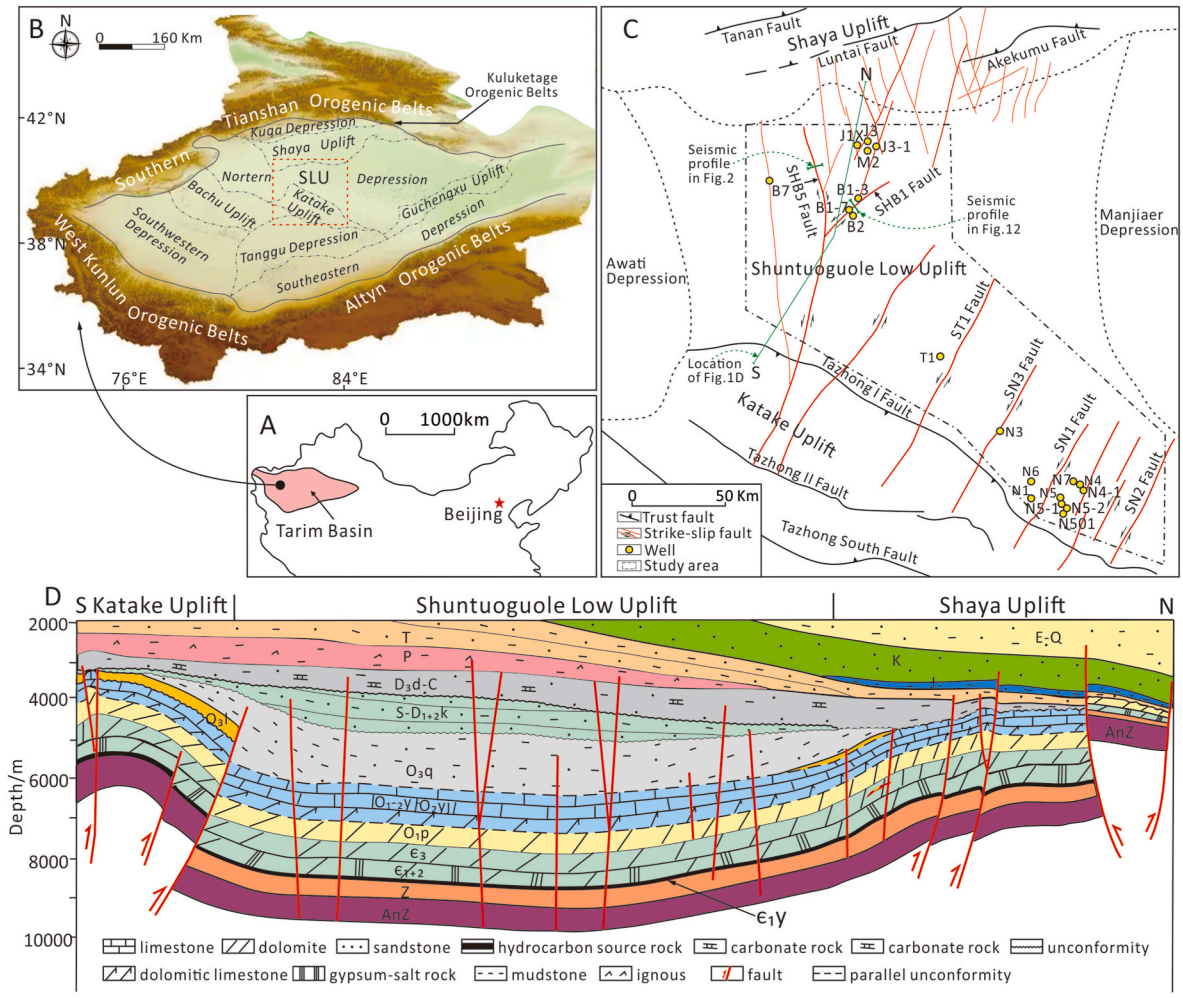

Fig. 1. Structural characteristics of the study area. (A) Location of the Tarim Basin in northwest China. (B) Orogenic belts around the Tarim Basin and tectonic units and the location of the Shuntuoguole Low Uplift (SLU) in the Tarim Basin. (C) Structural characteristics, well locations, main strike-slip faults and study area of the SLU. (D) Structural units and characteristics of the study area in NS direction profile.

samples were thin sectioned and underwent cathodoluminescence (CL) at the State Key Laboratory of Deep Oil and Gas in China University of Petroleum (East China) to identify the occurrences and stages of MCCFs.

Five samples from 3 wells were collected for the in-situ carbonate U-Pb dating experiments, which was carried out using the GeoLasPro 193 nm ArF excimer laser ablation system and the Agilent 7900 ICP-MS in the John de Laeter Centre Laboratory at Curtin University, Australia. Seventy-three groups of test ages were obtained in MCCFs with different petrological characteristics. The instrument's laser beam spot had a diameter of 87 μm, with a laser energy density of 5 J/cm^2, and a pulse frequency of 8 Hz. Helium was used as the carrier gas for the ablation material, and NIST SRM 612 was used to maximize the signal-to-background intensity ratio of Pb and U. Isotope ratios and age errors were both 1σ. The measurement spots were selected as far as possible from inclusions, and the raw measurement data were processed offline using the ICPMSDDataCal program (Liu et al., 2010). Zircon age calculations, concordia diagram plotting, and weighted average age plotting were performed using the Isoplot program (Ludwig, 2003). Refer to Tang et al. (2022) for detailed instrument parameters and specific methods for in-situ trace element determination and in-situ U-Pb isotope analysis.

Twenty-five samples from 19 wells were collected for the 105 groups of REE and Sr isotope experiments. The in-situ microanalyses of rare earth elements (REE) and Sr isotope ratios from thin sections were conducted at the State Key Laboratory of Ore Deposit Geochemistry of the Chinese Academy of Sciences. The REE was used a GeoLasPro laser system and a Laser Ablation Inductively Coupled Plasma Mass Spectrometry (LA-ICP-MS) with the beam spot diameter of 50 μm at the. In order to obtain the REE of different stages of MCCFs, the analyses of calcites and dolomites were also based on the results of the CL. Taking the international standards of NIST SRM 610 and NIST SRM 612 as external calibration standards, the quantitative calculation was carried out by using multi-external standards and non-internal standard method, and the data off-line processing was completed by using ICPMSDataCal software (Liu et al., 2010). The Sr isotope ratios were measured by a Neptune Plus MC-ICP-MS in combination with the aforementioned laser ablation system. According to the intensity of Sr content in the sample, the diameter of the laser spot varies between 60 and 180 μm. The testing standard uses the internal laboratory standard Coral-1. The data off-line processing was also conducted using ICPMS-DataCal (Liu et al., 2010). The interference correction method was after Tong et al. (2016).

Twenty-two samples from 16 wells were collected for the 70 groups of carbon and oxygen isotope experiments. CL microscope and micro-sampling system with 100 μm bit at China University of Petroleum (East China) were used to sample calcite and dolomite of different stages of MCCFs. CO_2 was extracted using the stepwise reaction method of Al-Aasm et al. (1990). The carbon and oxygen isotopes of CO_2 were analyzed using a mass spectrometer at the Chinese University of Geosciences (Wuhan). The Peedee belemnite (PDB) standard was used for

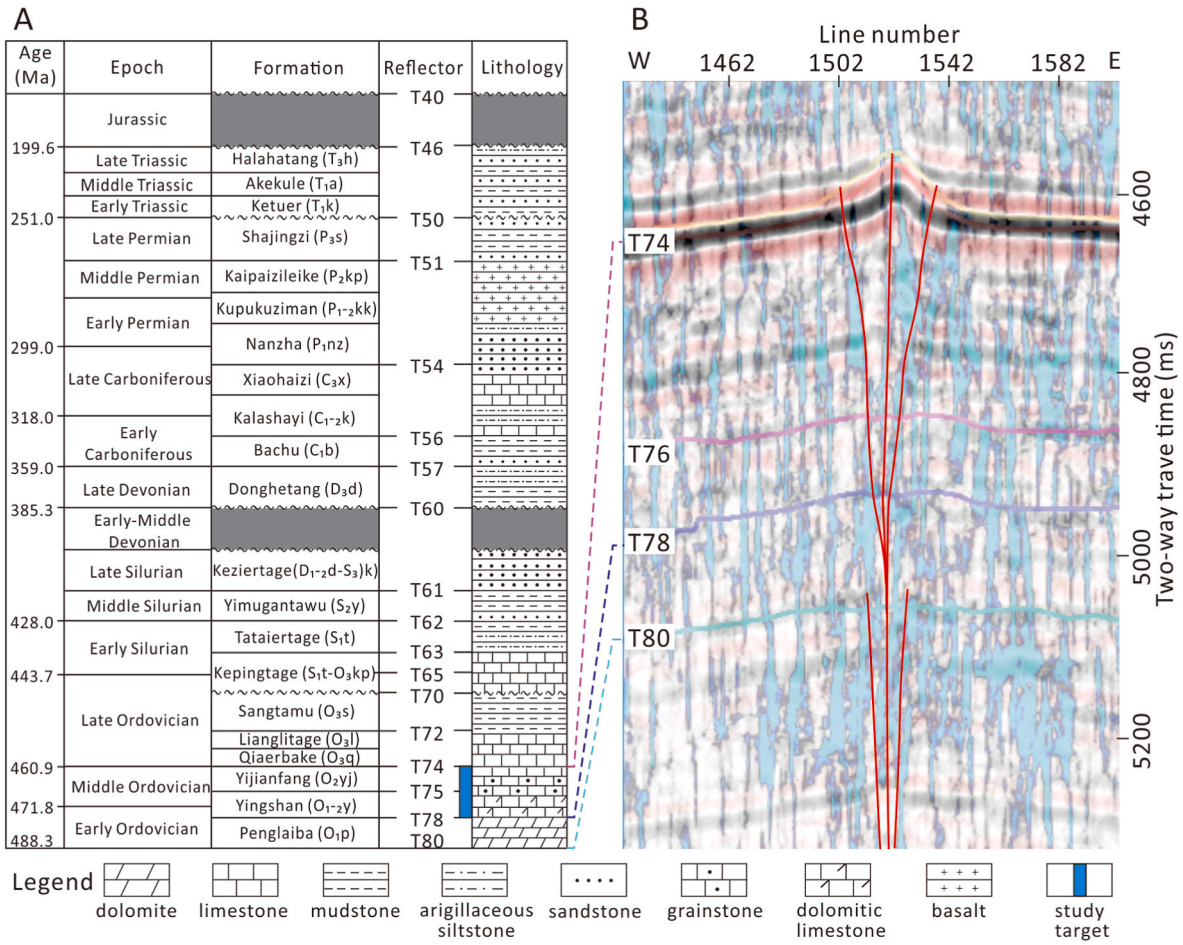

Fig. 2. Stratigraphy and structural characteristics of the Shuntuoguole low uplift (SLU) of the Middle-Upper Ordovician in the study area. (A) Schematic stratigraphy, seismic reflector, and lithology of the study area in the Tarim Basin. (B) Ant body attribute profile superimposed seismic profile show strike-slip faults and macro-fractures. See Fig. 1C for the location of seismic profile.

the carbon isotope analysis, while the standard mean ocean water (SMOW) standard was used for the oxygen isotope analysis. The precisions of the carbon and oxygen isotope ratios were ±0.2‰ and ±0.3‰, respectively. The oxygen isotope ratios using the PDB standard were calculated using the equation $\delta^{18}O_{v\text{-}SMOW} = 1.03086 \times \delta^{18}O_{v\text{-}PDB} + 30.86$.

4. Results

4.1. Characteristics and stages of MCCFs

Thin section analysis shows that there are mainly micro-structural fractures and sutures in the Middle-Upper Ordovician Yingshan and Yijianfang formations in the SLU. Minerals in MCCFs mainly include calcite and dolomite. The former mainly fills structural fractures, while the latter can be seen in both structural fractures and sutures.

4.1.1. Microfractures with calcite infilled (MFC)

MFC is widely distributed and have high abundance in grainstone, packstone and wackstone. MFC is usually corresponding with micro-structural fractures, with diverse shapes and occurrences. The study area mainly develops MFC with flat edges and relatively stable widths (Fig. 3A–C and 3H to J), MFC with curved edges and unidirectional or locally increased widths (Fig. 3D–G and K), and even reticular MFC (Fig. 3L). The width of MFC is usually between 30 and 500 μm. Calcite has a grain structure, a clean and bright surface, and is commonly produced in the form of embedded crystals (Fig. 3A–M). MFC exhibit characteristics of non-luminescence, orange-red or bright yellow luminescence under CL (Fig. 4).

There is obvious termination (Fig. 3E–H, K and 4E), cutting (Figs. 3J and 4A to B), and displacement (Fig. 3I to J and 4B to C) phenomena between MFC of different occurrences, and based on this, MFC can be divided into four stages. The first stage of MFC (C1) shows medium to coarse crystalline characteristics with no CL (Fig. 4A, B, D, F). The second stage of MFC (C2) exhibits bright yellow CL and terminates at C1 (Fig. 4A). The third stage of MFC (C3) exhibits orange-red or bright yellow CL. C3 cuts through C2 and C1, and disrupts C2 (Fig. 4A, B, C, E), and C3 is associated with fluorite (Fig. 4H and I). The fourth stage of MFC (C4) also shows orange-red CL, terminating at C3 (Fig. 4C–E) or surrounded by C3 and fluorite in the center of the fractures (Fig. 4H and I).

4.1.2. Microfractures with dolomite infilled (MFD)

Compared to MFC, MFD has a lower frequency of occurrence and can be seen in grainstone, packstone and wackstone. MFD are often filled with micro-structural fractures or distributed along suture lines. The width of MFD is generally between 50 and 800 μm, and dolomite has a good euhedral degree. Incomplete replaced carbonate grains or sparry calcite can be seen in MFD (Fig. 3D). According to the size of dolomite, MFD can be divided into two stages (D1 and D2). D1 mainly composes of powder-fine crystal dolomites with a small amount of saddle dolomite (Fig. 3M, N) and D2 is dominated by medium-coarse crystal dolomites (Fig. 3D–K, N, O). D1 commonly distributes along suture lines with irregular shape and a shorter extension distance (Fig. 3K–N and 4D, G).

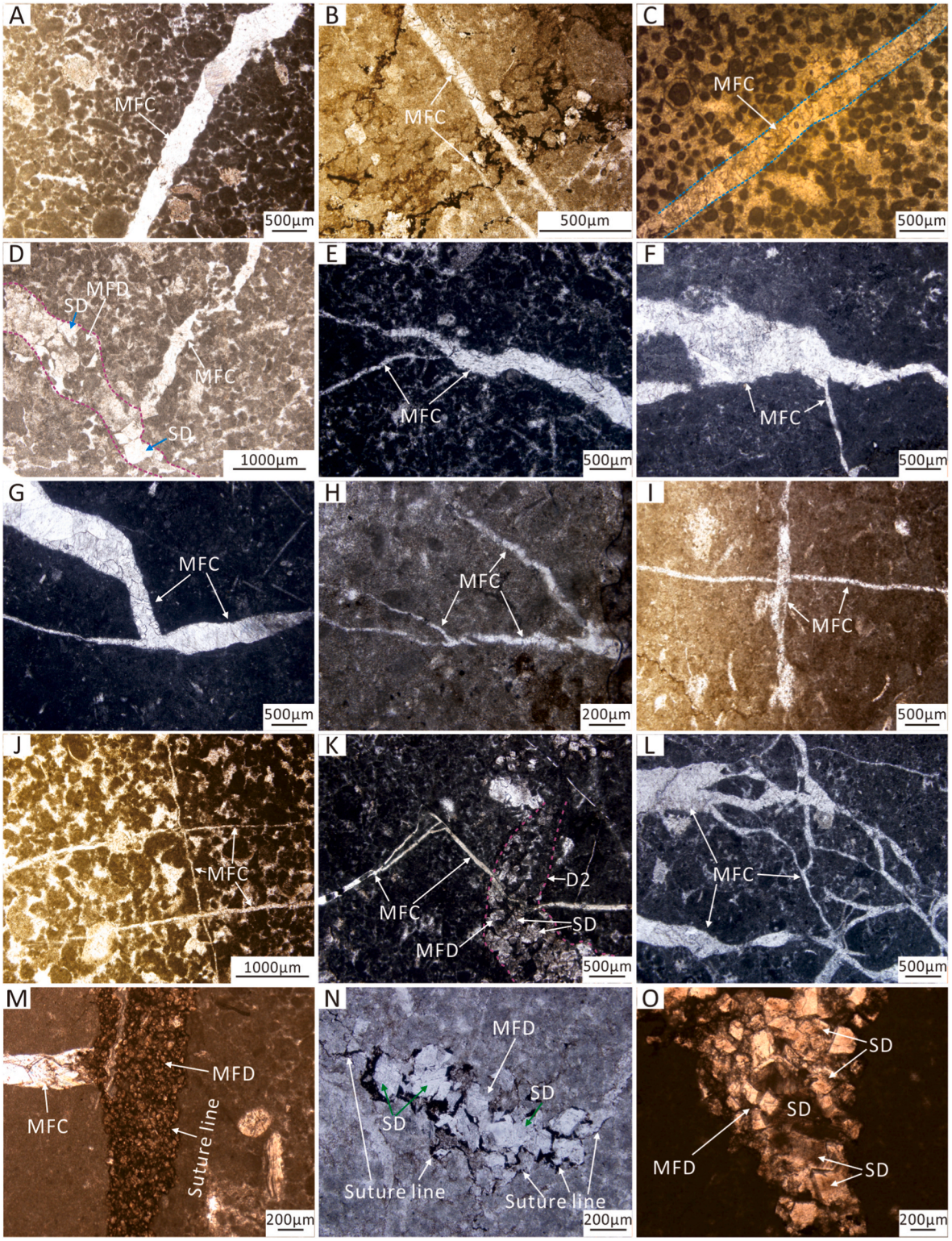

Fig. 3. Thin section observations show the types and occurrences of MCCFs in the Ordovician Yingshan and Yijianfang formations in the SLU. (A) MFC in grainstone from well N4-1 at 6569.68m. (B) MFC in packstone from well N5-2 at 6620m. (C) MFC in grainstone from well B2 at 7443m. (D) MFC and MFD with saddle dolomite in grainstone from well N5-1 at 7004.2m. MFC ends at MFD. (E) Two stages of MFC in packstone from well T1 at 7862.84m. Late MFC ends at early one. (F) Two stages of MFC in wackstone from well N7 at 6579.03m. Late MFC ends at early one. (G) Two stages of MFC in wackstone from well M2 at 7216.8m. Late MFC ends at early one. (H) Two stages of MFC in packstone from well B1-3 at 7320m. Late MFC end at early one. (I) Two stages of MFC in wackstone from well N4-1 at 6562.1m. Early MFC is staggered by late one. (J) Two stages of MFC in grainstone from well J3 at 7187.04m. Early MFC are staggered by late one. (K) Two stages of MFC and MFD with saddle dolomite in packstone from well N7 at 7100.3m. Late MFC ends at early one, and the early MFC is staggered by MFD. (L) Reticulated MFC in packstone from well T1 at 7863.65m. (M) MFC and MFD with powder fine crystalline dolomite in packstone from well N7 at 6578.4m. MFC ends at MFD. (N) MFD along suture line in wackstone from well N501 at 6350.75m. (O) MFD with saddle dolomite in mudstone from well N5 at 6785.1m.

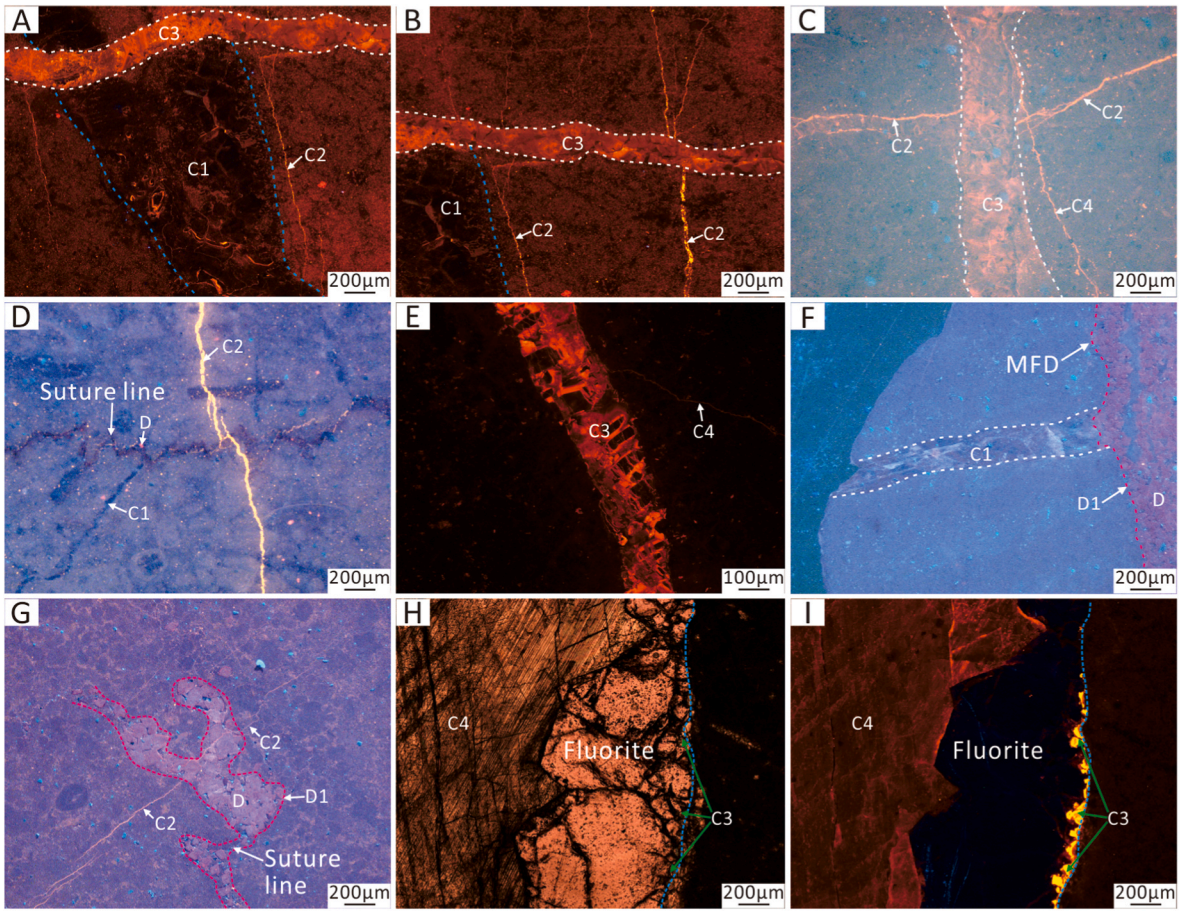

Fig. 4. CL images show the occurrences and stages of MCCFs in the Ordovician Yingshan and Yijianfang formations in the SLU. (A) and (B) Three stages of MFC (C1, C2, C3) from well J1X at 7260.96m (Wang et al., 2024). The second stage of MFC (C2) ends at the first stage of MFC (C1), the third stage of MFC cuts through the C1 and C2. (C) Three stages of MFC from well N5 at 6784.8m. C2 is staggered by C3, the fourth stage of MFC (C4) ends at C3. (D) Three stages of MFC from well B2 at 7441.5m. C1 ends at the MFD with powder dolomite (D1), C2 cuts through D1. (E) Two stages of MFC from well N6 at 6845.51m. C4 ends at C3. (F) Two stages of MCCF from well B1-7 at 7349.86m. C1 ends at D1. (G) Two stages of MCCF from well N4-1 at 6697.65m. C2 cuts through D1. (H) and (I) Two stages of MFC (C3 and C4) and fluorite from well J1X at 7260.99m.

D2 is usually corresponding with micro-structural fractures and has a generally flat edge and a longer extension distance (Fig. 3D–M, O and 4F). Saddle dolomite with higher abundance exist in the D2 (Fig. 3D–K, N, O). MFD has purple CL characteristics, while the CL color of D2 is relatively light than that of the D1 (Fig. 4D–F, G).

Thin section microscopic and CL images indicate that there are various contact relationships between MFC and MFD. For example, MFC terminates at MFD (Fig. 3D–M and 4D, F), MFC is disrupted by MFD (Fig. 3K), and MFC cuts through MFD (Fig. 4D–G).

4.2. Geochemical characteristics of MCCFs

4.2.1. U-Pb isotope dating

The U-Pb dating data shows that the formation times of the C1, C2, and C3 are 445.73 ± 3.26 Ma (Fig. 5A), 430.87 ± 2.07 Ma (Figs. 5B), and 255.1 ± 40.9 Ma (Fig. 5C), respectively. No effective age data for the C4 was obtained. The formation times of the D1 and D2 are 462 ± 13Ma (Figs. 5D) and 358 ± 17Ma (Fig. 5E), respectively.

4.2.2. In-situ REE compositions

The in-situ REE compositions of MCCFs analyzed by Laser Ablation Inductively Coupled Plasma Mass Spectrometry (LA-ICP-MS) are summarized in Table 1. The UCC normalized REE distributions of MCCFs are shown in Fig. 6. The REE of the intergranular sparry calcite is characterized by gentle distribution and δEu negative anomaly (Figs. 6A and 7 and Table 1). The C1 has the typical right-dip REE distribution, obvious LREE enrichment, δEu negative anomaly and high $(La/Yb)_N$ value characteristics (Figs. 6A and 7 and Table 1). The gentle REE distribution and $(La/Yb)_N$ value of the C2 are similar to those of the intergranular sparry calcite, but the C2 has a strong δEu negative anomaly (Figs. 6B and 7 and Table 1). The REE characteristics of the C3 occur as left-dip distribution, HREE enrichment, δEu positive anomaly and low $(La/Yb)_N$ value (Figs. 6C and 7 and Table 1). The C4 has similar REE distributions to that of the C3 (Fig. 6C and D), but the LREE/HREE and $(La/Yb)_N$ value of the C4 is higher than those of the C3 (Fig. 7 and Table 1). The δEu of the C4 is dominated by positive anomaly with a small amount of negative anomaly (Fig. 7). The content of REE in MFD is low, and both of the distribution patterns of D1 and D2 are gentle (Fig. 6E to F). The D1 with powder-fine crystal dolomites has an apparent δEu negative anomaly, and the D2 has a strong δEu positive anomaly (Fig. 6E to F and 7). The $(La/Yb)_N$ value of D1 is higher than that of D2 (Table 1).

4.2.3. Sr isotopic characteristics

The Sr isotopic composition of MCCFs is summarized in Table 2 and Fig. 8. The $^{87}Sr/^{86}Sr$ value of the Mid-Late Ordovician seawater is in the range of 0.7085–0.7088 (Veizer et al., 1999). The $^{87}Sr/^{86}Sr$ value of the intergranular sparry calcite is in the range of $^{87}Sr/^{86}Sr$ value of the Mid-Late Ordovician seawater. The $^{87}Sr/^{86}Sr$ value of the C1 with an average of 0.70984 is higher than that of the Mid-Late Ordovician seawater. The $^{87}Sr/^{86}Sr$ value of the C2 with an average of 0.70848 is

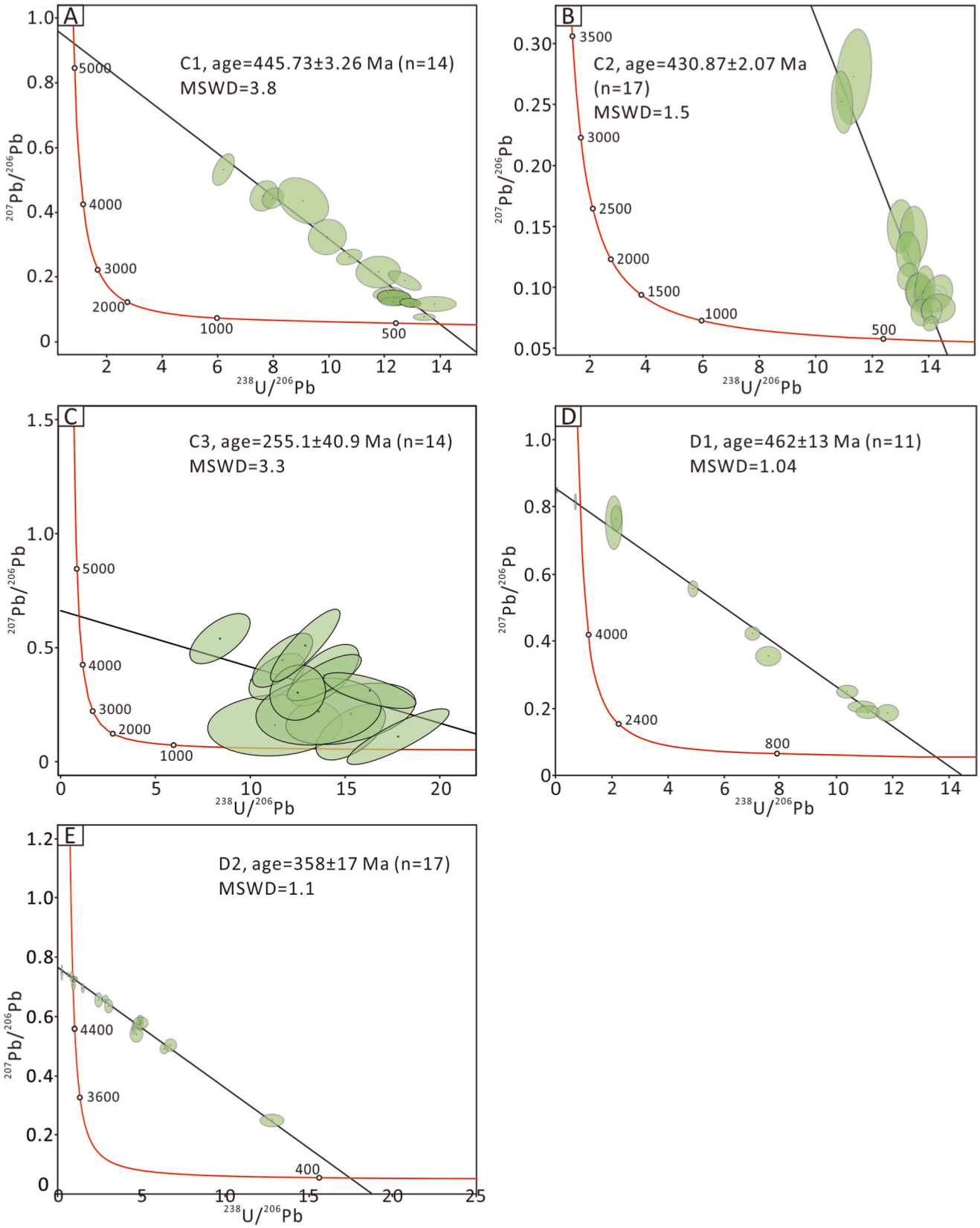

Fig. 5. U-Pb Tera-Wasserburg discordia (model-1) plots for the MFC and MFD in the Ordovician Yingshan and Yijianfang formations in the SLU. The results are reported as age = T ± X, where T is the age or initial Pb-ratio, X is the standard error. (A) U-Pb plots for C1 from well BP2H at 7536.05 m. (B) U-Pb plots for C2 from well B2 at 7520.82 m. (C) U-Pb plots for C3 from well N7 at 6487.5 m. (D) U-Pb plots for D1 from well N7 at 6487.3 m. (E) U-Pb plots for D2 from well N7 at 6487.3 m.

Table 1
Summary of LA-ICP-MS in-situ REE compositions of MCCFs and seawater cement calcite of the Ordovician Yingshan and Yijingfang formations in the SLU.

	C 1	C 2	C 3	C 4	D1	D2	SCC
La	1.8886	1.3129	0.8244	0.4974	0.4413	0.2465	0.3442
Ce	2.7851	1.8773	1.7564	0.9485	0.9594	0.4211	0.6254
Pr	0.2558	0.2183	0.2460	0.1109	0.1084	0.0476	0.0762
Nd	0.8389	0.8858	1.1364	0.4889	0.4328	0.1889	0.2956
Sm	0.1176	0.1653	0.2690	0.1121	0.0978	0.0342	0.0590
Eu	0.0175	0.0290	0.0672	0.0224	0.0125	0.0114	0.0100
Gd	0.0852	0.1587	0.3185	0.1136	0.0737	0.0407	0.0497
Tb	0.0112	0.0213	0.0475	0.0173	0.0107	0.0031	0.0070
Dy	0.0668	0.1286	0.3057	0.0988	0.0631	0.0274	0.0463
Ho	0.0141	0.0273	0.0654	0.0220	0.0125	0.0063	0.0049
Er	0.0368	0.0745	0.1754	0.0581	0.0349	0.0112	0.0192
Tm	0.0046	0.0100	0.0245	0.0089	0.0042	0.0058	0.0025
Yb	0.0310	0.0674	0.1588	0.0508	0.0302	0.0158	0.0178
Lu	0.0048	0.0107	0.0229	0.0076	0.0034	0.0048	0.0032
Y	0.3966	1.0332	2.6784	0.8684	0.3188	0.2060	0.3217
$(La/Yb)_N$	5.8335	1.3163	0.6308	0.9548	1.0706	0.7860	1.3715
δEu	0.8271	0.7599	1.2126	1.0613	0.6901	2.0416	0.8504
LREE	5.9036	4.4886	4.2995	2.1802	2.0521	0.9497	1.4105
HREE	0.2545	0.4985	1.1186	0.3771	0.2327	0.1150	0.1506
∑REE	6.1581	4.9872	5.4181	2.5573	2.2849	1.0647	1.5611
LREE/HREE	26.2512	8.6163	5.0154	7.5197	8.8171	5.6384	9.1349

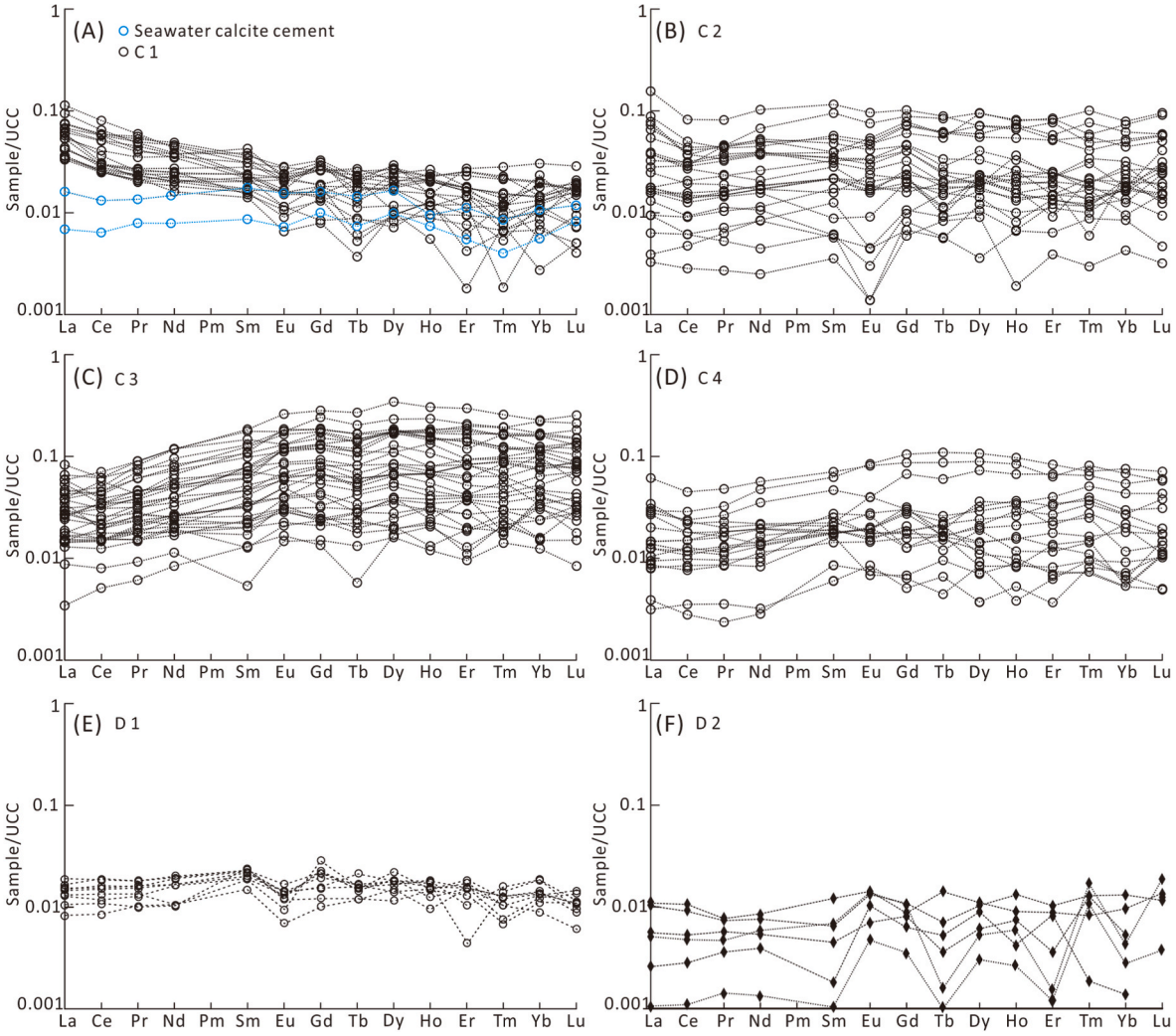

Fig. 6. UCC normalized REE distributions of MCCFs in the Ordovician Yingshan and Yijianfang formations in the SLU.

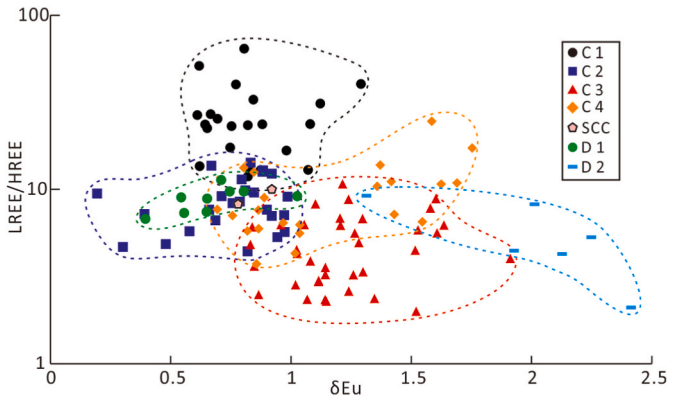

Fig. 7. Cross plot showing the δEu and LREE/HREE of MCCFs in the Ordovician Yingshan and Yijianfang formations in the SLU.

slightly lower than that of the Mid-Late Ordovician seawater. The $^{87}Sr/^{86}Sr$ value of the C3 with an average of 0.70781 is lower than that of the Mid-Late Ordovician seawater. The average $^{87}Sr/^{86}Sr$ values of the C4 (0.70853), intergranular sparry calcite (0.70867) and the Mid-Late Ordovician seawater are consistent, but the range of $^{87}Sr/^{86}Sr$ value of the C4 is larger than that of the latter two. The $^{87}Sr/^{86}Sr$ values of D1 (av. 0.70856) are also similar to those of the Mid-Late Ordovician seawater and intergranular sparry calcite. The $^{87}Sr/^{86}Sr$ values of D2 (av. 0.71241) are significantly higher than that of the Mid-Late Ordovician seawater.

4.2.4. Carbon and oxygen isotopic characteristics

The $\delta^{13}C_{PDB}$ and $\delta^{18}O_{PDB}$ compositions of MCCFs are summarized in Table 2 and Fig. 9. The $\delta^{13}C_{PDB}$ of the intergranular sparry calcite cement, C1, and C4 has almost the same range, but the $\delta^{13}C_{PDB}$ of the SCC is slightly heavier (Table 2). The $\delta^{13}C_{PDB}$ of the C2 is the lightest among all micro-carbonate veins (Fig. 9). The $\delta^{13}C_{PDB}$ of the C3 is slightly lighter that of the C1 and C4. D1 has a lighter $\delta^{13}C_{PDB}$ than that of the D2, but both of them are within the ranges of $\delta^{13}C_{PDB}$ of the C1, C3, and C4 (Fig. 9). The intergranular sparry calcite cement and D1 have relatively heavy $\delta^{18}O_{PDB}$ compositions (Fig. 9). C1 has the lightest $\delta^{18}O_{PDB}$ among all kinds of the micro-carbonate veins (Table 2 and Fig. 9). The $\delta^{18}O_{PDB}$ of C2 is within the same range as C3 and C4, but the $\delta^{18}O_{PDB}$ of C3 is slightly lighter. The D2 has a $\delta^{18}O_{PDB}$ composition lighter than that of the D1 and heavier than that of the C1-C4 (Fig. 9).

5. Discussion

5.1. Precipitation sequence of MCCFs

The formation order of MFC obtained through contact relationship (Fig. 4) is consistent with the precipitation time of MFC obtained through U-Pb dating (Fig. 5A–C). Although U-Pb dating did not obtain the age of C4, the contact relationship between C4 and C3 indicates that its formation occurred later than C3 (Fig. 3C). Both thin section microscopy and CL images show that C1 terminates at D1 and C2 cuts through D1 (Figs. 3M and 4D–F, G), indicating that the precipitation time of D1 is earlier than that of C1 and C2, which is consistent with the U-Pb dating results (Fig. 6A, B, D). The phenomenon of D2 cutting off C2 can be seen in the thin section microscopic image (Fig. 3K), indicating that D2 formed later than C2, which is consistent with the U-Pb dating results (Fig. 5B–E). Therefore, the precipitation sequence of MCCFs in the study area is D1, C1, C2, D2, C3, and C4.

5.2. Related fluids in the precipitation of MCCFs

The precipitation of carbonate cements in carbonate rocks can be formed during syndepositional, shallow burial, deep burial, and supergene periods, and their related fluids may be closely correlated with various types of fluids such as seawater, meteoric water, organic acids,

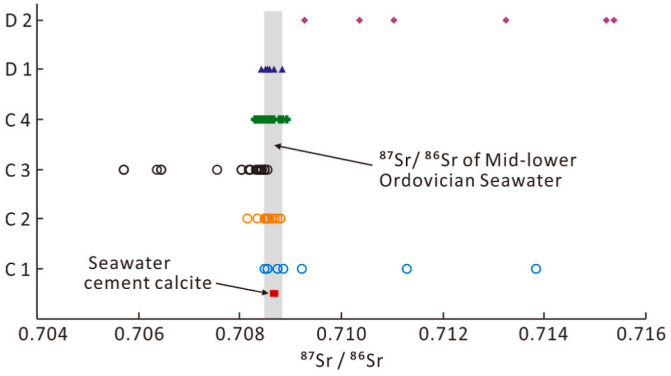

Fig. 8. $^{87}Sr/^{86}Sr$ values of Mid-Late Ordovician seawater, MCCFs and intergranular sparry calcite in the Ordovician Yingshan and Yijianfang formations in the SLU.

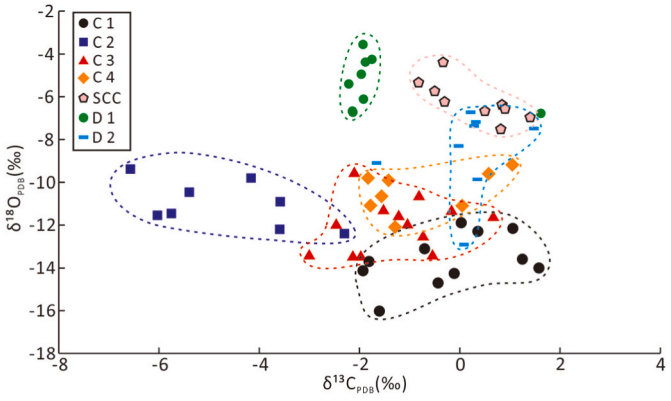

Fig. 9. Cross plot of the $\delta^{13}C_{PDB}$ and $\delta^{18}O_{PDB}$ of MCCFs and intergranular sparry calcite in the Ordovician Yingshan and Yijianfang formations in the SLU.

Table 2
Summary of strontium, carbon and oxygen isotopic compositions of MCCFs and seawater cement calcite of the Ordovician Yingshan and Yijingfang formations in the SLU.

	87Sr/86Sr				$\delta^{13}C_{v\text{-}PDB}$			$\delta^{18}O_{v\text{-}PDB}$		
	Min	Max	Mean	Error	Min	Max	Mean	Min	Max	Mean
SCC	0.70866	0.70868	0.70867	0.000057	−0.82	1.40	0.28	−7.52	−4.40	−6.21
C1	0.70806	0.71382	0.70984	0.000046	−1.93	1.58	−0.18	−16.02	−11.03	−13.41
C2	0.70814	0.70903	0.70848	0.000058	−6.57	−2.30	−4.67	−12.40	−9.38	−11.02
C3	0.70569	0.70851	0.70781	0.000043	−3.00	0.67	−1.38	−13.50	−9.58	−12.08
C4	0.70829	0.70889	0.70853	0.000055	−1.83	1.05	−0.78	−12.10	−9.18	−10.43
D1	0.70842	0.70881	0.70856	0.000056	−2.21	1.62	−1.61	−6.78	−3.56	−5.32
D2	0.70926	0.71535	0.71241	0.000081	−1.66	1.48	0.17	−12.90	−6.67	−8.40

hot brine, and deep hydrothermal fluids (Liu et al., 2017; Jiang et al., 2018; Han et al., 2019; Jiang, 2022; Wang et al., 2022, 2024).

The intergranular sparry calcite in carbonate rocks is closely related to the cementation of seawater, and is usually formed in the submarine phreatic zone where pore water frequently exchanges with normal seawater (Longman, 1980). The $^{87}Sr/^{86}Sr$ values of intergranular sparry calcite are highly consistent with that of the Mid-Late Ordovician seawater (Figs. 8 and 10), and its $\delta^{13}C_{PDB}$ is agree with that of typical marine carbonate rocks (Jansa and Noguera, 1990). Moreover, the REE distribution pattern of the intergranular sparry calcite has good consistency with the Ordovician Yingshan and Yijianfang formations (Wang et al., 2022). All of these indicate that the related fluid of the precipitation of intergranular sparry calcite in the Mid-Late Ordovician Yingshan and Yijianfang formations in the study area was seawater (Fig. 10).

U-Pb dating indicates that C1 precipitated during the late stage of the Late Ordovician Sangtamu Formation. At that time, the study area experienced a brief tectonic uplift, and the top of the Ordovician underwent a certain degree of erosion (Zhang et al., 2013; Wu et al., 2020a). The Mid-Upper Ordovician underwent a short period of supergene meteoric water action (Wu et al., 2021). Compared with SCC, the C1 has obvious LREE enrichment characteristics (Figs. 6 and 7), and $(La/Yb)_N$ value is as high as 5.8335 (Fig. 9), which reflect the obvious fractionation between LREE and LREE in C1 (Webb et al., 2008). Compared with LREE, HREE has a stronger migration ability in solution (Henderson, 1984; Aubert et al., 2002). Therefore, the enrichment of LREE suggests that the precipitation of C1 was affected by meteoric water (Aubert et al., 2002; Webb et al., 2008). The C1 exhibits a significant negative drift characteristic of $\delta^{18}O_{PDB}$ (Fig. 9), and high temperature or meteoric water participation are important factors causing negative oxygen isotope drift in calcite (Watkins et al., 2014; Wang et al., 2016). However, the precipitation time of C1 indicates that the formation was shallowly buried at that time, excluding the influence of high temperature, which further suggests that the related fluids of C1 precipitation were influenced by meteoric water. The $^{87}Sr/^{86}Sr$ values of some C1 are significantly higher than those of the SCC and Mid-Upper Ordovician seawater (Figs. 8 and 10), indicating that the precipitation of C1 was influenced by the ^{87}Sr-rich fluid (Mountjoy et al., 1992; Qing and Mountjoy, 1994). The T70 interface in the study area suffered erosion, and meteoric water infiltrated along the strike-slip fault connecting the surface, fully leaching the mudstone of the Upper Ordovician Sangtamu Formation, providing a high $^{87}Sr/^{86}Sr$ value fluid for the precipitation of C1 (Fig. 10; Denison et al., 1998).

U-Pb dating shows that the precipitation time of the C2 was in the Late Caledonian. At that time, the first stage of oil and gas filling occurred in the platform basin area of the Tarim Basin, and a large amount of oil and gas and organic acids entered the Mid-Lower Ordovician Yingshan and Yijianfang formations (Li et al., 2010; Wu et al., 2013; Lu et al., 2020). The significant negative drift characteristic of $\delta^{13}C_{PDB}$ composition of C2 (Fig. 9) indicates that its precipitation process was influenced by organic fluids (Mack et al., 1991; Pearson and Nelson, 2005; Sensula et al., 2006; Wang et al., 2016, 2018, 2021, 2024). Eu^{3+} is difficult to be reduced to Eu^{2+} under normal temperature background (Bau et al., 2010; Frei et al., 2017). Organic matter deposited and preserved in reduction environment often shows apparently negative δEu anomaly characteristics, and the organic fluid generated by it also has negative δEu anomaly (Feng et al., 2008, 2009; Himmler et al., 2010). Therefore, the strong negative δEu anomaly of the C2 further indicates the influence of organic fluids on its precipitation (Table 1, Figs. 6B and 7). The REE distribution pattern and $(La/Yb)_N$ value and $^{87}Sr/^{86}Sr$ value of the C2 are similar to those of the seawater cement calcite (Figs. 8 and 10A to B), indicating that the source of Ca^{2+} for the C2 precipitation came from the dissolution of calcites already existed in the early stage or carbonate rocks by organic acids (Fig. 10).

U-Pb dating shows that the precipitation time of the C3 is the development period of Permian Large Igneous Province in Tarim Basin (Ma et al., 2013). The $\delta^{18}O_{PDB}$ of the C3 exhibits significant negative drift characteristics (Fig. 9), and the burial depth of the Mid-Upper Ordovician has exceeded 3000m, indicating that the C3 precipitation process may have been affected by high temperatures (Watkins et al., 2014; Wang et al., 2016, 2024). Magmatic hydrothermal fluids are usually characterized by HREE enrichment (Mills and Elderfield, 1995). Most of the $(La/Yb)_N$ values of C3 are less than one, indicating significant enrichment characteristics of HREE (Fig. 7). High temperature has reduction effect on Eu^{3+}, and enrichment of Eu^{2+} makes the positive δEu anomaly (Michard and Albarede, 1986; Olivarez and Owen, 1991; Bau and Dulski, 1999; Wu et al., 2007; Debruyne et al., 2016; Robbins et al., 2016). The δEu characteristics of the C3 are agree with those of magmatic hydrothermal fluid (Figs. 6C and 7), which reflects that the precipitation of C3 was affected by magmatic hydrothermal fluid. The C3 has a significant low $^{87}Sr/^{86}Sr$ value (Figs. 8 and 10), indicating that its precipitation process was influenced by ^{87}Sr-poor mantle derived fluids (Banner, 1995; Qing et al., 1998). The $^{87}Sr/^{86}Sr$ value of C3 (av. = 0.70781) is higher than that of mantle ferromagnesian rocks (av. = 0.704), indicating that the contact between the magmatic hydrothermal and the Cambrian clastic rock during the upwelling process increased the ^{87}Sr-rich characteristics of C3-forming fluids (Mountjoy et al., 1992;

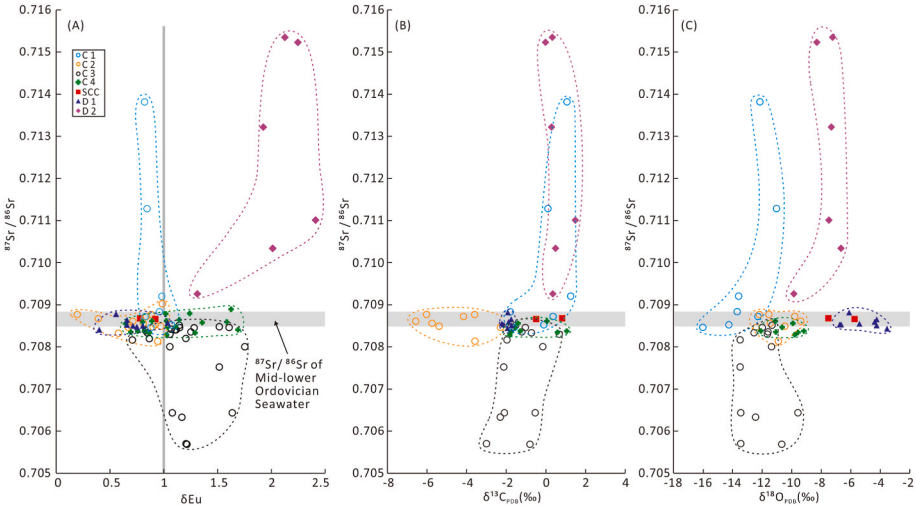

Fig. 10. Geochemical differences of MCCFs and intergranular sparry calcite in the Ordovician Yingshan and Yijianfang formations in the SLU. (A) Cross plot of the δEu and $^{87}Sr/^{86}Sr$ of MCCFs and intergranular sparry calcite. (B) Cross plot of the $\delta^{13}C_{PDB}$ and $^{87}Sr/^{86}Sr$ of MCCFs and intergranular sparry calcite. (C) Cross plot of the $\delta^{18}O_{PDB}$ and $^{87}Sr/^{86}Sr$ of MCCFs and intergranular sparry calcite.

Banner, 1995). However, due to the fast-upward speed of magmatic fluids, they cannot fully contact the clastic rock, so the C3 precipitation related fluids retain the ^{87}Sr-poor characteristics (Fig. 10). The coexistence of 3 with magmatic hydrothermal minerals such as fluorite further indicates that mantle derived magmatic hydrothermal fluids influenced its precipitation process (Fig. 4H and I; Subías and Fernández-Nieto, 1995)Previous studies have also obtained evidence of hydrothermal fluid through geochemical analysis of calcite in fractures from adjacent areas (Ukar et al., 2020; Wang et al., 2022), indicating the universality of hydrothermal activity in the platform-basin area.

Although the absolute age of C4 has not been obtained, the REE distribution pattern of the C4 is similar to that of the C3 (Fig. 6C and D), indicating that the C4 and C3 had similar material sources (Taylor and Mclennan, 1985). The major positive δEu anomaly further suggests that the magmatic hydrothermal fluid influenced the precipitation of the C4 (Table 1 and Fig. 7). The $(La/Yb)_N$ value of the C4 is slightly higher than that of the C3 (Table 1), which suggest that the related fluid in the C4 precipitation should be a mixture of the terminal fluid of the magmatic hydrothermal fluid and the formation water. The average $^{87}Sr/^{86}Sr$ value of C4 is within the range of Mid-Late Ordovician seawater (Veizer et al., 1999), but C4 has a wider $^{87}Sr/^{86}Sr$ value (Fig. 8), further indicating that the dissolution of wall rocks and early precipitated calcite may provide material sources for the precipitation of C4. The $\delta^{13}C_{PDB}$ of C4 is consistent with C3, but the negative drift degree of $\delta^{18}O_{PDB}$ of C4 is lower than that of C3 (Figs. 9 and 10), further indicating that the precipitation process of C4 is influenced by the mixing of hydrothermal and formation fluids (Watkins et al., 2014; Wang et al., 2016). Therefore, the C4 precipitation fluid may be related to the thorough mixing of deep magmatic hydrothermal fluids and formation fluids or dissolution of early existing calcite.

U-Pb dating indicates that the precipitation time of D1 was during the late stage of the Yijianfang Formation to the early stage of the Upper Ordovician. At that time, the Yingshan and Yijianfang formations buried shallowly (Han et al., 2019; Wang et al., 2022, 2024). The REE distribution pattern of fine-grained dolomite in D1 is similar to that of seawater cemented calcite (Fig. 6A–E), and both have similar δEu and $(La/Yb)_N$ values (Figs. 7 and 9). The $^{87}Sr/^{86}Sr$ values of fine-grained dolomite in D1 (av. = 0.70856), Mid-Late Ordovician seawater and seawater cemented calcite are in the same range (Figs. 8 and 10). These all indicate that the D1 precipitation fluid was closely related to seawater. The $\delta^{13}C_{PDB}$ and $\delta^{18}O_{PDB}$ ranges of D1 are consistent with those of the Ordovician dolomite formed in shallow burial depth of the Tarim Basin (Figs. 9 and 10; Veizer et al., 1999; Guo et al., 2017), which further indicates that the formation of D1 may be related to seawater concentration in the shallow burial period. D1 is mainly distributed along sutures, without accompanying evaporates or exposed structures, also indicating that the formation of D1 may be corresponding to shallow burial dolomitization (Guo et al., 2017).

The U-Pb dating indicates that the D2 precipitation time was during the Late Devonian-Early Carboniferous. D2 is mainly composed of saddle dolomite, with typical δEu positive anomaly and HREE enrichment characteristics (Figs. 6F and 7), and the $(La/Yb)_N$ value is close to C3, indicating that the D2 precipitation process was influenced by high-temperature fluids (Davies and Smith, 2006; Yang et al., 2022a,b). The $^{87}Sr/^{86}Sr$ values of D2 are significantly different from those of C3. The $^{87}Sr/^{86}Sr$ values of D2 are higher than those of Ordovician seawater (Figs. 8 and 10), indicating that although the precipitation processes of D2 and C3 may be influenced by hydrothermal fluids, there may be differences in their fluid sources. Previous studies have shown that mantle derived magmatic hydrothermal fluids in the study area have Si-rich and F-rich characteristics (Wang et al., 2022, 2024). Due to the lack of Mg^{2+}, magmatic hydrothermal fluids cannot cause large-scale hydrothermal dolomitization in the Mid-Lower Ordovician. Therefore, the D2 precipitation fluid is not closely related to magmatic hydrothermal fluids. In addition to magmatic hydrothermal fluid, hot brine from the deep strata also developed in the Tarim Basin, such as interlayer hot brine of Cambrian evaporates (Cai et al., 2001, 2008; Wang et al., 2022). Most of the hot brine was inherited from marine source fluid sealed in carbonate and sulfate rocks (Cai et al., 2001), which can provide sufficient Mg^{2+} for the precipitation of D2 (Boschetti et al., 2020). The Cambrian interlayer hot brine fully contacts with rocks rich in terrestrial detrital materials such as mudstone, gypsum mudstone, and mudstone in the evaporative platform, resulting in high $^{87}Sr/^{86}Sr$ values (Davies and Smith, 2006; Cai et al., 2008). Cambrian saddle dolomite affected by Cambrian hot brine has typical δEu positive anomaly and high $^{87}Sr/^{86}Sr$ value characteristics, and its carbon and oxygen isotopes (av. $\delta^{18}O_{PDB} = -8.9‰$, av. $\delta^{13}C_{PDB=}-0.88‰$) is consistent with D2 (Table 2 and Fig. 9). Therefore, the D2 precipitation fluid may be related to the Cambrian interlayer hot brine. Meanwhile, saddle dolomites occurred in D1 indicate that the Cambrian hot brine may also influence the transformation of powder-fine grained dolomite in D1.

The precipitation time and sequence of MCCFs record the intrusion time and evolution process of geological fluids in the Ordovician carbonate reservoirs in the study area. Therefore, the geological fluid evolution process recorded by MCCFs in the Yingshan and Yijianfang formations was concentrated seawater, meteoric water, organic acids, Mg-rich hot brine, Si and F-rich magmatic hydrothermal fluid, and mixed fluid of magmatic hydrothermal fluid and formation water (Fig. 11). The diverse types and geochemical differences of geological fluids and their corresponding MCCFs suggest that there was still fluid activity during the deep burial process of the tight Ordovician carbonate rocks in the platform-basin area of the Tarim Basin.

5.3. *Structure-fluid coupled evolution of Ordovician in the platform-basin area*

The statistical results of igneous rock age of orogenic belts around the Tarim Basin show that the subduction of the West Kunlun Ocean occurred in the Cambrian-Early Ordovician, and the uplift of the West Kunlun orogenic belt caused by collision closure mainly occurred in the Middle Ordovician-Silurian (Yuan et al., 2002; Zhang et al., 2019). The Altyn ocean subduction mainly occurred during the Cambrian-Middle Ordovician, and the collision closure and mountain uplift mainly occurred during the Late Ordovician-Devonian (Meng et al., 2013; Dong et al., 2018). The eastern section of the Southern Tianshan Ocean subduction occurred during the Silurian-Early Devonian, and the collision closure formed mountains during the Mid-Late Carboniferous (Zhang et al., 2017). The western section of the Southern Tianshan Ocean subduction occurred during the Silurian-Early Carboniferous, and the collision closure occurred during the Late Carboniferous-Early Permian (Gao et al., 2009; Ren et al., 2017).

The connection between the Tarim Block and the Paleo-Asian and Tethyan tectonic systems results in a unified regional dynamic background between the Tarim Block and the peripheral orogenic belts (Wang et al., 2020b). The Tarim Block has a rigid characteristic, and the convergence or dispersion of plate edges is the source of internal tectonic stress in the craton (Xu et al., 2011). This also provides a dynamic background for the formation of strike-slip faults and related structural fractures in the basin (Wang et al., 2020a, 2020b), as well as the activity of geological fluids (Fig. 12).

The precipitation time of D1 is consistent with that of calcite cements filled in macrofractures within the fault zone obtained by previous researchers, and the related fluids are all related to seawater (Veizer et al., 1999; Guo et al., 2017). During the Episodes I-III of the middle Caledonian Orogeny, the Tarim block was located between 10 °S and 25 °S (Fig. 12; Domeier and Torsvik, 2014; Domeier, 2018). In the Middle Ordovician, the ancient Kunlun Ocean began to subduct, and the West Kunlun terrane entered a collision and collage stage with the Tarim block. The passive continental margin in the southern part of the Tarim turned to the active continental margin (Li et al., 2018; Zhang et al., 2018, 2019), and the Tarim block entered a regional compression stage.

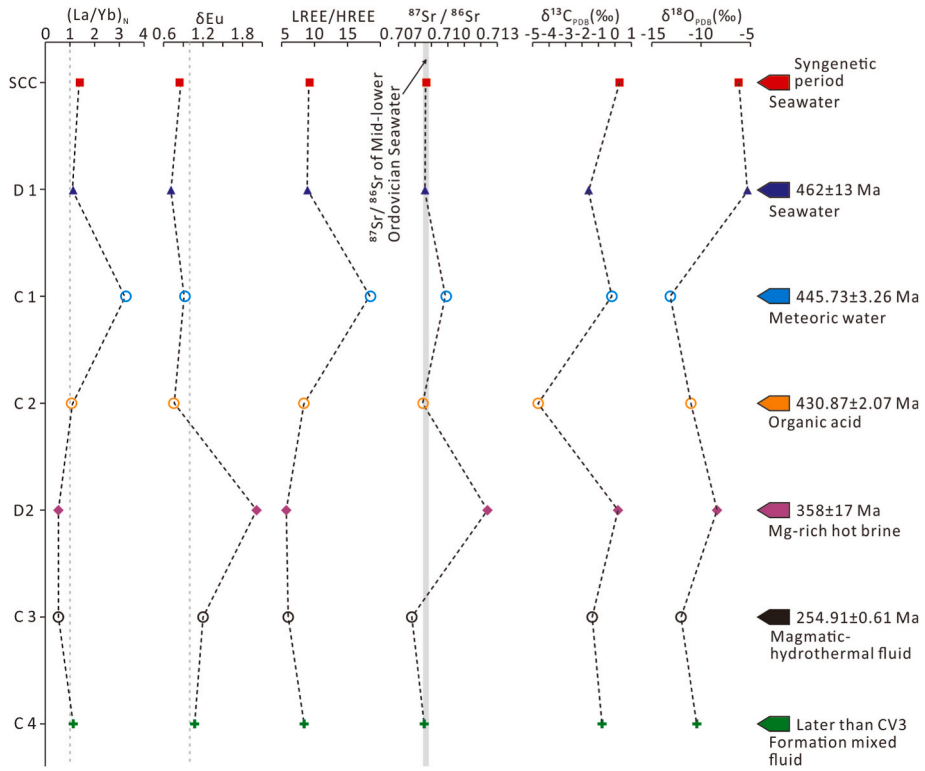

Fig. 11. Types, geochemical characteristics and timing of diagenetic fluids in the Ordovician Yingshan and Yijianfang formations in the SLU.

The northeast oriented compression stress from the southwest edge had been the main stress in the inner basin (Wu et al., 2018, 2020 ab, 2021). Under this stress, the Tazhong ancient uplift lifted, forming a large northwest trending fault-uplift (Wu et al., 2018). Affected by the remote compressive stress of the southwestern plate edge, the overall structure of the study area was gentle, and the Yingshan and Yijianfang formations were stably deposited (Tang et al., 2014). In the late stage of the middle Caledonian (End of the middle Ordovician), a collision occurred between the southeastern part of the Tarim block and the Qaidam block, leading to the closure of the South Altyn Ocean (Dong et al., 2018), resulting in strong northwest compressive stress from the southeastern edge of the basin. Meanwhile, the ancient Kunlun Ocean on the southwestern edge began to close (Li et al., 2018; Zhang et al., 2017, 2018, 2019), and the compressive stress on the southwestern edge continued to increase (Fig. 12). At this time, the northern part of the block was resisted by the South Tianshan oceanic crust, forming a reaction force from north to south, but the stress was relatively weak (Zhang et al., 2017). The stress generated by block edge activity was mainly transmitted to the interior of the basin through horizontal stress (Wu et al., 2018, 2020 ab, 2021). Under the influence of horizontal compressive stresses in different directions and sizes in the southwest, southeast, and north of the basin, the strike-slip fault system in the study area began to develop (Fig. 12). Due to the relatively small scale of strike-slip fault in the early stage, the corresponding structural fractures in carbonate rocks of the Yingshan and Yijianfang formations was limited (Wu et al., 2018, 2020 ab, 2021). The precipitation of powder-fine grained dolomites was not related to the structural fractures, but the tectonic activity might cause the migration of concentrated seawater along suture lines. The precipitation time of D1 is in good agreement with the activity of strike-slip fault at the end of the middle Ordovician (Figs. 12 and 13), which furtherly indicates the formation of the D1 is closely related to the activity of strike-slip faults and regional tectonic movements (Fig. 12). At this time, the Yijianfang Formation was in a shallow burial stage (Tang et al., 2014), and the seawater sealed in the formation was concentrated and transported along suture lines, resulting in local shallow burial dolomitization in the limestone (Fig. 12).

At the end of the Episodes III of the middle Caledonian Orogeny (Terminal Ordovician), the orogenic movements on the southern and northern margins of the basin continued. The ancient Tianshan Ocean in the north strongly subducted towards the central Tianshan block, while the western Kunlun block in the south and the Tarim block continued to collide strongly (Yuan et al., 2002; Gao et al., 2009; Ren et al., 2017; Zhang et al., 2017, 2019). The Altyn tectonic domain in the southeast margin was strongly folded and orogenic, causing the Tarim block to be compressed from multiple directions around the basin (Dong et al., 2018). The entire basin was in a strong compression environment, the NE trending strike-slip faults in SLU began to develop on a large scale based on early faults, forming a series of faults with relatively wide fault cores and fracture zones (Wu et al., 2020a, Wang et al., 2024). Influenced by the above orogenic activities, the Ordovician in the study area was risen and eroded at the top (Wu et al., 2020a), and the strike-slip fault communicated with the surface (T70 reflector) (Fig. 12; Wang et al., 2024). The forming-fluid of C1 was meteoric water, and the precipitation time was consistent with the erosion time of the Ordovician, indicating that C1 recorded the structure and fluid response in the Ordovician in the study area formed by the Episode III of the Caledonian Orogeny (Fig. 12).

During the late Caledonian Orogeny, the Tarim block was located between 0° and 15°N (Domeier and Torsvik, 2014; Domeier, 2018). The orogenic movement at the southern edge of the Tarim block ended, and the subduction of the South Tianshan Ocean weakened and gradually closed, but continued to transmit compressive stress into the block (Gao et al., 2009; Ren et al., 2017; Zhang et al., 2017, 2019). At this time, the North Altyn orogeny at the southeastern edge of the basin was strong, and the interior of the basin was subjected to strong compressive stress from the southeast direction (Dong et al., 2018). The NE trending strike-slip faults continued to be active, forming a series of en echelon distributed faults in the Upper Ordovician and Silurian, and the strike-slip faults communicated downwards with the source rocks of the Yuertus Formation (Wu et al., 2020a; Wang et al., 2024). The first stage

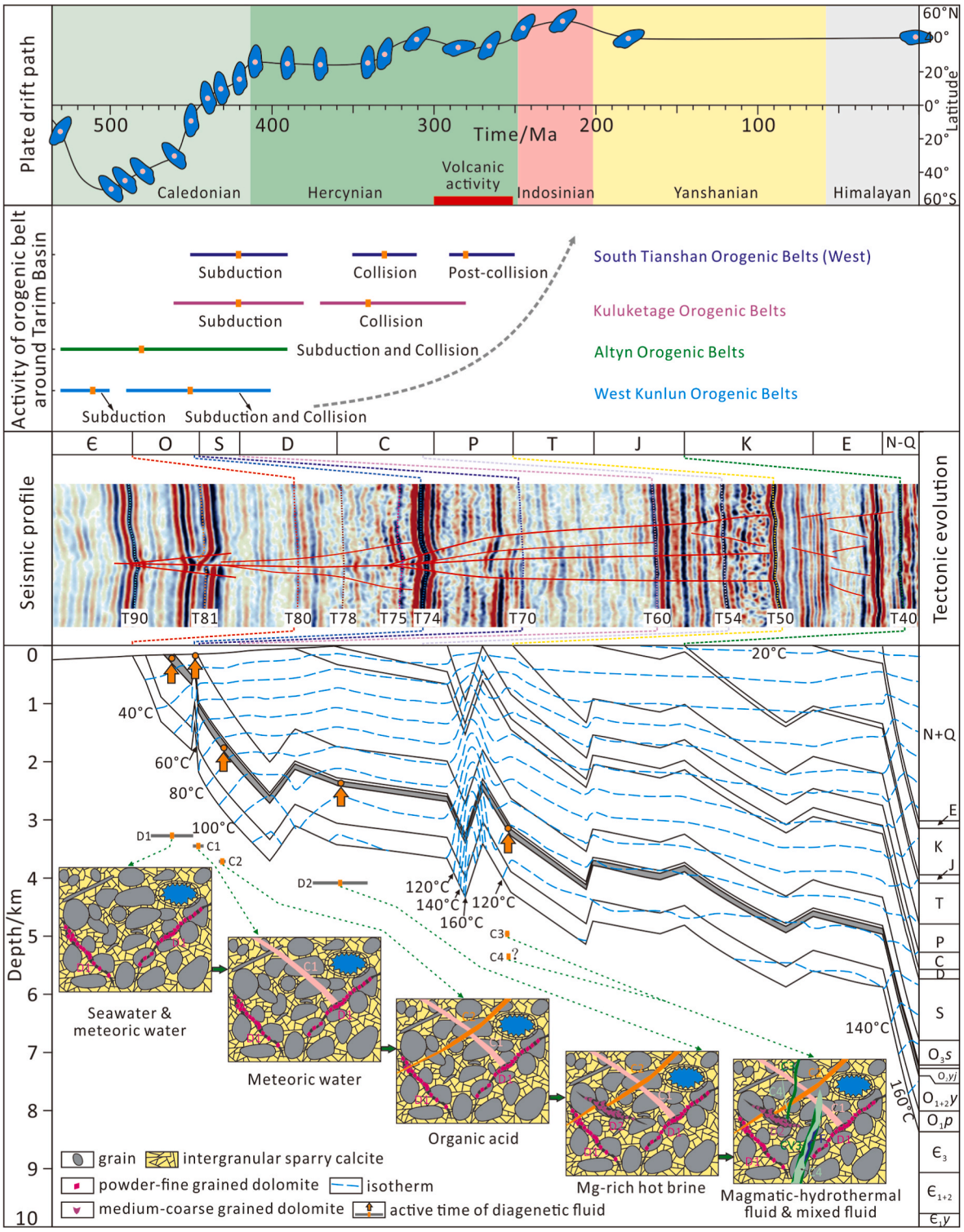

Fig. 12. Coupling evolution of tectonic movements and diagenetic fluids and formation of corresponding MCCFs in the Ordovician Yingshan and Yijianfang formations in the SLU of the Tarim Basin. The activity time of the West Kunlun Orogenic Belts is after Zhang et al. (2019). The activity time of the Altyn Orogenic Belts is after Dong et al. (2018). The activity time of the Kulugetage Orogenic Belts is after Zhang et al. (2017). The activity time of the West South Tianshan Orogenic Belts is after Ren et al. (2017). The plate drift path was after Domeier and Torsvik (2014) and Domeier (2018). The burial and thermal history was modified from Yang et al. (2021). Affected by the activities of the surrounding orogenic belt, the Tarim Basin undergone complex and varied stress evolution, which led to the development of multiple stages of strike-slip fault activities and complex fault-fracture system in the basin. Through petrographic and geochemical analysis, multi-stage microfractures consistent with strike-slip fault activity and surrounding orogenic movements were discovered, and their fillings simultaneously recorded fluid activity that matched tectonic activity.

of oil and gas filling occurred in the study area (Li et al., 2010; Wu et al., 2013; Lu et al., 2020). When organic acids entered the Ordovician Yingshan and Yijianfang formations accompanied by oil and gas, they participated in the precipitation of micro-carbonate veins of C2 (Fig. 12).

In the early stage of the Hercynian Orogeny, the Tarim block was located between 20°N and 25°N (Domeier and Torsvik, 2014; Domeier, 2018). Due to the closure of the North Kunlun Ocean in the southern part of the Tarim block during the late Devonian and the subduction of the South Tianshan Ocean in the northern part of the block, the continental margin orogeny was strong (Gao et al., 2009; Ren et al., 2017; Zhang et al., 2017). Due to the greater influence of compressive and torsional stress caused by the subduction of the Southern Tianshan Ocean, the study area was influenced by compressive stress from the north, and the strike-slip fault was inherited and developed based on the fault formed by the Caledonian Orogeny (Fig. 12; Wu et al., 2018). The precipitation time of D2 is 358 ± 17Ma, which is consistent with the tectonic movement and the strike-slip fault activity during the late Devonian in the study area, indicating a close relationship between the formation of D2 and regional tectonic movement (Fig. 12). At the end of the Devonian, the burial depth of the Cambrian gypsum-salt rock reached 5000m, and the formation temperature reached 140 °C (Cai et al., 2001, 2008). Tectonic movement made the strike-slip faults connect the Cambrian gypsum-salt rock in the study area (Wu et al., 2018). The sealed high-temperature Mg-rich hot brine surged up along the fault into the fractures of the Yingshan and Yijianfang formations, causing local hydrothermal dolomitization, forming D2 mainly composed of saddle dolomite (Fig. 12).

In the middle-late stages of the Hercynian Orogeny, the Tarim block was located between 25°N and 40°N (Domeier and Torsvik, 2014; Domeier, 2018). Since the late Carboniferous, the central and northern Tarim Basin was in the stress relaxation stage after the West Kunlun and Altyn orogenies (Dong et al., 2018; Zhang et al., 2019). Meanwhile the southern Tianshan area was also in the temporary tension stage at this time, so a regional tensile stress field was formed (Gao et al., 2009; Ren et al., 2017; Zhang et al., 2017), resulting in a large area of volcanic rocks in the early-middle Permian to erupt in a fissure style, forming the Permian igneous province in the Tarim Basin (Fig. 12; Ma et al., 2013). The continental collision orogeny in the western part of the southern Tianshan Mountains occurred at about 299~250 Ma (Gao et al., 2009; Ren et al., 2017). The fault activity of the Tarim Basin in the late Permian generally migrated from the southern part of the basin to the northern part (Wu et al., 2018). The strike-slip fault system in the study area has inherited activities (Wu et al., 2021). Magmatic hydrothermal fluid entered the Yingshan and Yijianfang formations along the fault zone and fracture system, forming C3 (Fig. 12). At the same time, the study area experienced the second stage of oil and gas charging (Ma et al., 2013; Wang et al., 2024). As the magmatic hydrothermal fluid mixed with the formation fluid, the fluid temperature decreased and might form C4 (Fig. 12).

At the end of the Triassic, the South Tianshan orogeny almost ended (Ren et al., 2011). Since the Jurassic, the Tabei area had been in the stress relaxation stage after the South Tianshan orogeny, and regional tectonic extension occurred (Deng et al., 2019). The entire study area was still in the NNW oriented tensile and torsional stress field, and the strike-slip fault undergone inherited sinistral tensile and torsional. During the late Yanshan-early Himalayan, due to the Himalayan orogeny, the Tarim block escaped and rotated clockwise (Zhang et al., 2013), and the entire study area was still in an NWW oriented tensile and torsional stress field, forming an NNE trending dextral extensional torsional normal fault. However, the impact of strike-slip fault activity on the Yingshan and Yijianfang formations was relatively small (Wu et al., 2021); no micro-carbonate vein records related to the Indosinian, Yanshan, and Himalayan orogenies were found in the samples. Studies have shown that the Yingshan and Yijianfang formations in the study area experienced the third stage of hydrocarbon (mainly gas) charging during the Himalayan orogeny (Ma et al., 2013).

6. Conclusions

(1) According to the occurrence, interrelationships, and U-Pb dating of MCCFs, there are four stages of MFC and two-stages of MFD in the Ordovician Yingshan and Yijianfang formations in the SLU. The formation order of these MCCFs is D1, C1, C2, D2, C3, and C4. MCCFs recorded the evolution of geofluids during the burial process of carbonate rocks in the study area, including seawater, meteoric water, organic acids, Mg-rich hot brine, magmatic hydrothermal fluids, and mixed fluids of hydrothermal fluids and formation fluids.

(2) The precipitation times of MCCFs have a good correspondence with orogeny around the Tarim Basin and active times of strike-slip faults in the platform basin area. The formation of D1, C1, C2, D2, C3, and C4 in the Ordovician Yingshan and Yijianfang formations in the SLU was consistent with the tectonic activities and corresponding fluids in the late Middle Ordovician, late Ordovician, late Caledonian orogeny, early Hercynian and Mid-late Hercynian, respectively. This not only indicates a close connection between fluid activity and tectonic activity in sedimentary basins, but also confirms that the formation of MCCFs in carbonate formations is closely related to regional tectonic-fluid coupling activities. This study provides a good example for studying macro-scale tectonic-fluid coupling activities in basins using MCCFs.

CRediT authorship contribution statement

Jian Wang: Writing – original draft, Supervision, Project administration, Investigation, Funding acquisition, Conceptualization. **Dongping Tan:** Writing – original draft, Software, Methodology, Data curation. **Yingchang Cao:** Supervision, Resources, Project administration, Investigation, Funding acquisition, Conceptualization. **Jun Han:** Software, Resources, Investigation, Formal analysis. **Haijun Yang:** Resources, Methodology, Investigation, Data curation. **Yin Liu:** Writing – original draft, Software, Methodology, Formal analysis. **Keyu Liu:** Writing – review & editing, Supervision, Project administration, Conceptualization.

Declaration of competing interest

The authors declare that they have no known competing financial interests or personal relationships that could have appeared to influence the work reported in this paper.

Acknowledgements

This work was co-funded by the Natural Science Foundation of China (Grant Nos. 42172146 and 41821002), the Taishan Scholars Program of the Shandong Province (Grant No. tsqn202312111), the National Key Research and Development Program of China (Grant No. 2022YFE0203400), and the Fund of State Key Laboratory of Deep Oil and Gas, China University of Petroleum (East China) (Grant No. SKLDOG2024-ZYRC-05). We are also grateful to Northwest Oil Field Company (Sinopec) and the PetroChina Tarim Oilfield Company for permission to access their in-house databases.

Data availability

Data will be made available on request.

References

Al-Aasm, I.S., Taylor, B.E., South, B., 1990. Stable isotope analysis of multiple carbonate samples using selective acid extraction. Chem. Geol. 80, 119–125. https://doi.org/10.1016/0168-9622, 90.

Anders, M.H., Laubach, S.E., Scholz, C.H., 2014. Microfractures: a review. J. Struct. Geol. 69, 377–394. https://doi.org/10.1016/j.jsg.2014.05.011.

Aubert, D., Stille, P., Probst, A., Gauthier-Lafaye, F., Pourcelot, L., Nero, M.D., 2002. Characterization and migration of atmospheric REE in soils and surface water. Geochim. Cosmochim. Acta.Geochim. Cosmochim. Acta. 66, 3339–3350. https://doi.org/10.1016/S0016-7037(02)00913-4.

Banner, J.L., 1995. Application of the trace element and isotope geochemistry of strontium to studies of carbonate diagenesis. Sedimentology 42, 805–824. https://doi.org/10.1111/j.1365-3091.1995.tb00410.x.

Baqués, V., Ukar, E., Laubach, S.E., Forstner, S.R., Fall, A., 2020. Fracture, dissolution, and cementation events in ordovician carbonate reservoirs, Tarim Basin, NW China. Geofluids 243, 1–28. https://doi.org/10.1155/2020/9037429.

Barbier, M., Hamon, Y., Callot, J.P., Floquet, M., Daniel, J.M., 2012. Sedimentary and diagenetic controls on the multiscale fracturing pattern of a carbonate reservoir: the Madison formation (Sheep Mountain, Wyoming, USA). Mar. Pet. Geol.Mar. Pet. Geol. 29, 50–67. https://doi.org/10.1016/j.marpetgeo.2011.08.009.

Barker, S.L.L., Bennett, V.C., Cox, S.F., Norman, M.D., Gagan, M.K., 2009. Sm▪Nd, Sr, C and O isotope systematics in hydrothermal calcite-fluorite veins: implications for fluid-rock reaction and geochronology. Chem. Geol. 268, 58–66. https://doi.org/10.1016/j.chemgeo.2009.07.009.

Bau, M., Dulski, P., 1999. Comparing yttrium and rare earths in hydrothermal fluids from the Mid-Atlantic Ridge: implications for Y and REE behaviour during near-vent mixing and for the Y/Ho ratio of Proterozoic seawater. Chem. Geol. 155, 77–90. https://doi.org/10.1016/S0009-2541(98)00142-9.

Bau, M., Balan, S., Schmidt, K., Koschinsky, A., 2010. Rare earth elements in mussel shells of the Mytilidae family as tracers for hidden and fossil high-temperature hydrothermal systems. Earth Planet Sci. Lett. 299, 310–316. https://doi.org/10.1016/j.epsl.2010.09.011.

Becker, S.P., Eichhubl, P., Laubach, S.E., Reed, R.M., Lander, R.H., Bodnar, R.J., 2010. A 48 M.Y. History of fracture opening, temperature, and fluid pressure: cretaceous travis peak formation, east Texas basin. Geol. Soc. Am. Bull. 122, 1081–1093.

Bons, P.D., Elburg, M.A., Gomez-Rivas, E., 2012. A review of the formation of tectonic veins and their microstructures. J. Struct. Geol. 43, 33–62. https://doi.org/10.1016/j.jsg.2012.07.005.

Boschetti, T., Awadh, S.M., Al-Mimar, H.S., Iacumin, P., Toscani, L., Selmo, E., Yaseen, Z. M., 2020. Chemical and isotope composition of the oilfield brines from Mishrif Formation (southern Iraq): diagenesis and geothermometry. Mar. Pet. Geol. 122, 104637. https://doi.org/10.1016/j.marpetgeo.2020.104637.

Cai, C., Franks, S.G., Aagaard, P., 2001. Origin and migration of brines from Paleozoic strata in Central Tarim, China: constraints from 87Sr/86Sr, δD, δ18O and water chemistry. Appl. Geochemistry 16, 1269–1284. https://doi.org/10.1016/S0883-2927(01)00006-3.

Cai, C.F., Li, K.K., Li, H.T., Zhang, B.S., 2008. Evidence for cross formational hot brine flow from integrated 87Sr/86Sr, REE and fluid inclusions of the Ordovician veins in Central Tarim, China. Appl. Geochemistry. 23, 2226–2235. https://doi.org/10.1016/j.apgeochem.2008.03.009.

Caja, M.A., Al-Aasm, I.S., Marfil, R., Tsige, M., Martin-Crespo, T., Salas, R., 2003. Multiphase carbonate cementation related to fractures in the upper jurassic limestones, maestrat basin (iberian range, Spain). J. Geochem. Explor. 78–79, 33–38. https://doi.org/10.1016/S0375-6742(03)00045-1.

Caja, M.A., Permanyer, A., Marfil, R., Al-Aasm, I.S., Martín-Crespo, T., 2006. Fluid flow record from fracture-fill calcite in the eocene limestones from the South ▪ pyrenean basin (NE Spain, and its relationship to oil shows. J. Geochem. Explor. 89, 27–32. https://doi.org/10.1016/j.gexplo.2005.11.009.

Cooley, M.A., Price, R.A., Kyser, T.K., Dixon, J.M., 2011. Stable-isotope geochemistry of syntectonic veins in Paleozoic carbonate rocks in the Livingstone Range anticlinorium and their significance to the thermal and fluid evolution of the southern Canadian foreland thrust and fold belt. Am. Assoc. Pet. Geol. Bull. 95, 1851–1882. https://doi.org/10.1306/01271107098.

Curtis, J.B., 2002. Fractured shale-gas systems. Am. Assoc. Pet. Geol. Bull. 86, 1921–1938.

Davies, G.R., Smith, L.B., 2006. Structurally controlled hydrothermal dolomite reservoir facies: an Overview. Am. Assoc. Pet. Geol. Bull. 90, 1641–1690. https://doi.org/10.1306/05220605164.

Debruyne, D., Hulsbosch, N., Muchez, P., 2016. Unraveling rare earth element signatures in hydrothermal carbonate minerals using a source-sink system. Ore Geol. Rev. 72, 232–252. https://doi.org/10.1016/j.oregeorev.2015.07.022.

Deng, S., Li, H., Zhang, Z., Zhang, J., Yang, X., 2019. Structural characterization of intracratonic strike-slip faults in the central Tarim Basin. Am. Assoc. Pet. Geol. Bull. 103, 109–137. https://doi.org/10.1306/06071817354.

Denison, R.E., Koepnick, R.B., Burke, W.H., Hetherington, E.A., 1998. Construction of the cambrain and ordovician seawater 87Sr/86Sr curve. Chem. Geol. 152, 325–340. https://doi.org/10.1016/s0009-2541(98)00119-3.

Ding, Z.W., Wang, R.J., Chen, F.F., Yang, J.P., Zhu, Z.Q., Yang, Z.M., Sun, X.H., Xian, B., Li, E.P., Shi, T., Zuo, C., Li, Y., 2020. Origin, hydrocarbon accumulation and oil-gas enrichment of fault-karst carbonate reservoirs: a case study of Ordovician carbonate reservoirs in South Tahe area of Halahatang oilfield, Tarim Basin. Pet. Explor. Dev+. 47, 306–317. https://doi.org/10.1016/S1876-3804(20)60048-9.

Dockrill, B., Shipton, Z.K., 2010. Structural controls on leakage from a natural CO_2 geologic storage site: central Utah, USA. J. Struct. Geol. 32, 1768–1782. https://doi.org/10.1016/j.jsg.2010.01.007.

Domeier, M., 2018. Early Paleozoic tectonics of Asia: towards a full-plate model. Geosci. Front. 9, 789–862. https://doi.org/10.1016/j.gsf.2017.11.012.

Domeier, M., Torsvik, T.H., 2014. Plate tectonics in the late Paleozoic. Geosci. Front. 5, 303–350. https://doi.org/10.1016/j.gsf.2014.01.002.

Dong, Y.P., He, D.F., Sun, S.S., Liu, X.M., Zhou, X.H., Zhang, F.F., Yang, Z., Cheng, B., Zhao, G.C., Li, J.H., 2018. Subduction and accretionary tectonics of the East Kunlun orogen, western segment of the Central China Orogenic System. Earth Sci. Rev. 186, 231–261. https://doi.org/10.1016/j.earscirev.2017.12.006.

Eichhubl, P., Boles, J.R., 2000. Focused fluid flow along faults in the monterey formation, coastal California. Geol. Soc. Am. Bull. 112, 1667–1679.

Ezati, M., Azizzadeh, M., Riahi, M.A., Fattahpour, V., Honarmand, J., 2018. Characterization of micro-fractures in carbonate Sarvak reservoir, Using petrophysical and geological data, SW Iran. J. Pet. Sci. Eng. 170, 675–695. https://doi.org/10.1016/j.petrol.2018.06.058.

Feng, D., Chen, D.F., Qi, L., Roberts, H.H., 2008. Petrographic and geochemical characterization of seep carbonate from Alaminos Canyon, Gulf of Mexico. Chin. Sci. Bull. 53, 1716–1724.

Feng, D., Chen, D.F., Roberts, H.H., 2009. Petrographic and geochemical characterization of seep carbonate from Bush Hill (GC 185, gas vent and hydrate site of the Gulf of Mexico. Mar. Pet. Geol. 26, 1190–1198. https://doi.org/10.1016/j.marpetgeo.2008.07.001.

Frei, R., Døssing, L.N., Gaucher, C., Boggiani, P.C., Frei, K.M., Bech Árting, T., Crowe, S. A., Freitas, B.T., 2017. Extensive oxidative weathering in the aftermath of a late Neoproterozoic glaciation—evidence from trace element and chromium isotope records in the Urucum district (Jacadigo Group, and Puga iron formations (Mato Grosso do Sul, Brazil). Gondwana Res. 49, 1–20. https://doi.org/10.1016/j.marpetgeo.2008.07.001.

Gao, J., Long, L.L., Reiner, K., Qian, Q., Liu, D.Y., Xiong, X.M., Su, W., Liu, W., Wang, Y. T., Yang, F.Q., 2009. Tectonic evolution of the South Tianshan orogen and adjacent regions, NW China: geochemical and age constraints of granitoid rocks. Int. J. Earth Sci. 98, 1221–1238. https://doi.org/10.1007/s00531-008-0370-8.

Gasparrini, M., Sassi, W., Gale, J.F.W., 2014. Natural sealed fractures in mudrocks: a case study tied to burial history from the Barnett Shale, Fort Worth Basin, Texas, USA. Mar. Pet. Geol. 55, 122–141. https://doi.org/10.1016/j.marpetgeo.2013.12.006.

Gomez, L.G., Laubach, S.E., 2006. Rapid digital quantification of microfracture populations. J. Struct.l Geol. 28, 1–13. https://doi.org/10.1016/j.jsg.2005.12.006.

Guo, X.W., Liu, K.Y., Jia, C.Z., Song, Y., Zhao, M., Zhuo, Q., Lu, X., 2016. Fluid evolution in the dabei gas field of the kuqa depression, Tarim Basin, NW China: implications for fault ▪ related fluid flow. Mar. Pet. Geol. 78, 1–16. https://doi.org/10.1016/j.marpetgeo.2016.08.024.

Guo, C., Chen, D.Z., Dong, S.F., Qian, Y.X., Liu, C.G., 2017. Early dolomitisation of the lower-middle ordovician cyclic carbonates in northern Tarim Basin, NW China. Sci. China Earth Sci. 60, 1283–1298. https://doi.org/10.1007/s00531-008-0370-8.

Han, X.Y., Deng, S., Tang, L.J., Cao, Z.C., 2017. Geometry, kinematics and displacement characteristics of strike-slip faults in the northern slope of Tazhong uplift in Tarim Basin: a study based on 3D seismic data. Mar. Pet. Geol. 88, 410–427. https://doi.org/10.1016/j.marpetgeo.2017.08.033.

Han, C.C., Lin, C.Y., Lu, X.B., Tian, J.J., Ren, L.H., Ma, C.F., 2019. Petrological and geochemical constraints on fluid types and formation mechanisms of the Ordovician carbonate reservoirs in Tahe Oilfield, Tarim Basin, NW China. J. Pet. Sci. Eng. 178, 106–120. https://doi.org/10.1016/j.petrol.2019.03.010.

Henderson, P., 1984. General geochemical properties and abundance of rare earth elements. Dev. Geochem. 2, 1–32. https://doi.org/10.1016/B978-0-444-42148-7.50006-X.

Himmler, T., Bach, W., Bohrmann, G., Peckmann, J., 2010. Rare earth elements in authigenic methane-seep carboantes as tracers for fluid composition during early diagenesis. Chem. Geol. 277, 126–136.

Hooker, J.N., Gale, J.F.W., Gomez, L.A., Laubach, S.E., Marrett, R., Reed, R.M., 2009. Aperture-size scaling variations in a low-strain opening-mode fracture set, Cozzette Sandstone, Colorado. J. Struct. Geol. 31 (7), 707–718. https://doi.org/10.1016/j.jsg.2009.04.001.

Hooker, J.N., Gomez, L.A., Laubacn, S.E., Gale, J.F.W., Marrett, R., 2012. Effects of diagenesis(cement precipitation)during fracture opening on fracture aperture-size scaling in carbonate rocks. Geol. Soc. Spec. Publ. 370, 187–206. https://doi.org/10.1144/SP370.9.

Jansa, L.F., Noguera, U.V.H., 1990. Geology and diagenetic history of over-pressured sandstone reservoirs, venture gas field, offshore Nova Scotia, Canada. Am. Assoc. Pet. Geol. Bull. 74, 1640–1658. https://doi.org/10.1306/0C9B2551-1710-11D7-8645000102C1865D.

Jiang, L., 2022. Diagenesis of the san andres formation in 1360 the seminole unit in central basin platform, western Texas. Am. Assoc. Pet. Geol. Bull. 106, 267–287. https://doi.org/10.1306/08092118042.

Jiang, L., Worden, R.H., Yang, C.B., 2018. Thermochemical sulphate reduction can improve carbonate petroleum reservoir quality. Geochim. Cosmochim. Acta. 223, 127–140. https://doi.org/10.1016/j.gca.2017.11.032.

Jin, Z.J., Cao, J., Hu, W.X., Zhang, Y.J., Yao, S.P., Wang, X.L., Zhang, Y.Q., Tang, Y., Shi, X.P., 2008. Episodic petroleum fluid migration in fault zones of the northwestern junggar basin (northwest China): evidence from hydrocarbon-bearing zoned calcite cement. Am. Assoc. Pet. Geol. Bull. 92, 1225–1243. https://doi.org/10.1306/06050807124.

Kareem, K.H., Al-Aasm, I.S., Mansurbeg, H., 2019. Structurally-controlled hydrothermal fluid flow in an extensional tectonic regime: a case study of cretaceous Qamchuqa Formation, Zagros Basin, Kurdistan Iraq. Sediment. Geol. 386, 52–78. https://doi.org/10.1016/j.sedgeo.2019.04.001.

Lander, R.H., Larese, R.E., Bonnell, L.M., 2008. Toward more accurate quartz cement models: the importance of euhedral versus noneuhedral growth rates. Am. Assoc. Pet. Geol. Bull. 92, 1537–1563. https://doi.org/10.1306/07160808037.
Laubach, S.E., 2003. Practical approaches to identifying sealed and open fractures. Am. Assoc. Pet. Geol. Bull. 87, 561–579. https://doi.org/10.1306/11060201106.
Laubach, S.E., Gale, J.F.W., 2006. Obtaining fracture information for low-permeability (tight) gas sandstones from sidewall cores. J. Petrol. Geol. 29, 147–158. https://doi.org/10.1111/j.1747-5457.2006.00147.x.
Leythaeuser, D., Krooss, B.M., 1996. Geofluids: origin, migration and evolution of fluids in sedimentary basins. J. Pet. Sci. Eng. 15, 395–396. https://doi.org/10.1016/0146-6380(95)90097-7.
Li, Q.M., Wu, G.H., Pang, X.Q., Pan, W.Q., Luo, C.S., Wang, C.L., Li, X.S., Zhou, B., 2010. Hydrocarbon accumulation conditions of ordovician carbonate in Tarim Basin. Acta Geol. Sin.–Engl. 84, 1180–1194.
Li, S.Z., Zhao, S.J., Liu, X., Cao, H.H., Yu, S., Li, X.Y., Somerville, L.D., Yu, S.Y., Suo, Y.H., 2018. Closure of the proto-tethys ocean and early paleozoic amalgamation of microcontinental blocks in east asia. Earth Sci. Rev. 186, 37–75.
Liu, Y.S., Hu, Z.C., Zong, K.Q., Gao, C.G., Gao, S., Xu, J., Chen, H.H., 2010. Reappraisement and refinement of zircon U-Pb isotope and trace element analyses by LA-ICP-MS. Chin. Sci. Bull. 55, 1535–1546. https://doi.org/10.1007/s11434-010-3052-4.
Liu, C.H., Wu, C.L., Gao, Y.H., Lei, M., Qin, H.P., 2016a. Age, composition, and tectonic significance of Palaeozoic granites in the Altynorogenic belt, China. Int. Geol. Rev. 58, 131–154. https://doi.org/10.1080/00206814.2015.1056757.
Liu, H., Somerville, I., Lin, C., Zuo, S., 2016b. Distribution of Palaeozoic tectonic superrimposed unconformities in the Tarim Basin, NW China: significance for the evolution of palaeogeomorphology and sedimentary response. Geol. J. 51, 627–651. https://doi.org/10.1002/gj.2664.
Liu, J.Q., Li, Z., Cheng, L.J., Li, J.W., 2017. Multiphase calcite cementation and fluids evolution of a deeply buried carbonate reservoir in the upper ordovician lianglitag formation, Tahe oilfield, Tarim Basin, NW China. Geofluids 1–19. https://doi.org/10.1155/2017/4813235.
Longman, M.W., 1980. Carbonate diagenetic textures from near surface diagenetic environment. Am. Assoc. Pet. Geol. Bull. 64, 461–487. https://doi.org/10.1007/s11434-010-3052-4.
Lu, X.B., Wang, Y., Tian, F., Li, X.H., Yang, D.H., Li, T., Lv, Y.P., He, X.M., 2017. New insights into the carbonate karstic fault system and reservoir formation in the Southern Tahe area of the Tarim Basin. Mar. Pet. Geol. 86, 587–605. https://doi.org/10.1016/j.marpetgeo.2017.06.023.
Lu, Z.Y., Li, Y.T., Ye, N., Zhang, S.N., Lu, C.J., Li, W., Cheng, Z., Ding, X.Q., Zhu, B., Huang, B.W., 2020. Fluid inclusions record hydrocarbon charge history in the Shunbei Area, Tarim Basin, NW China. Geofluids 12, 1–15. https://doi.org/10.1155/2020/8847247.
Ludwig, K.R., 2003. User's Manual for Isoplot 3.00: A Geochronological Toolkit for Microsoft Excel, vol. 4. Geochronology Centre Special Publication, Berkeley, p. 74.
Ma, X.X., Shu, L.S., Santosh, M., Li, J., 2013. Paleoproterozoic collisional orogeny in central tianshan: assembling the Tarim block within the columbia supercontinent. Precambrian Res. 228, 1–19.
Mack, G.H., Cole, D.R., Giordano, T.H., Schaal, W.C., Barcelos, J.H., 1991. Palaeoclimatic controls on stable oxygen and carbon isotopes in the caliche of the abo formation (Permian), south central, New Mexico, USA. J. Sediment. Petrol. 61, 458–472. https://doi.org/10.1306/D426773A-2B26-11D7-8648000102C1865D.
Marfil, R., Caja, M.A., Tsige, M., Al-Aasm, I.S., Martin-Crespo, T., Salas, R., 2005. Carbonate-cemented stylolites and fractures in the Upper Jurassic limestones of the Eastern Iberian Range, Spain: a record of palaeofluids composition and thermal history. Sediment. Geol. 178, 237–257. https://doi.org/10.1016/j.sedgeo.2005.05.010.
Marrett, R., Ortega, O.J., Kelsey, C.M., 1999. Extent of power-law scaling for natural fractures in rock. Geology 27 (9), 799–802.
Meng, F.C., Zhang, J.X., Cui, M.H., 2013. Discovery of early paleozoic eclogite from the east Kunlun, western China and its tectonic significance. Gondwana Res. 23, 825–836.
Michard, A., Albarede, F., 1986. The REE content of some hydrothermal fluids. Chem. Geol. 55, 51–60. https://doi.org/10.1016/0009-2541(86)90127-0.
Mills, R.A., Elderfield, H., 1995. Rare earth element geochemistry of hydrothermal deposits from the active TAG Mound, 26°N Mid-Atlantic Ridge. Geochim. Cosmochim. Acta. 59, 3511–3524. https://doi.org/10.1016/0016-7037(95)00224-n.
Morad, S., Al-Aasm, I.S., Sirat, M., Sattar, M.M., 2010. Vein calcite in cretaceous carbonate reservoirs of abu dhabi: record of origin of fluids and diagenetic conditions. J. Geochem. Explor. 106, 156–170. https://doi.org/10.1016/j.gexplo.2010.03.002.
Mountjoy, E.W., Qing, H., Mcnutt, R.H., 1992. Strontium isotopic composition of Devonian dolomites, Western Canada Sedimentary Basin: significance of sources of dolomitizing fluids. Appl. Geochemistry. 7, 59–75. https://doi.org/10.1016/0883-2927(92)90015-U.
Nothdurft, L.D., Webb, G.E., Kamber, B.S., 2004. Rare earth element geochemistry of late devonian reefal carbonates, canning basin, western Australia: confirmation of a seawater REE proxy in ancient limestones. Geochim. Cosmochim. Acta. 68, 263–283. https://doi.org/10.1016/S0016-7037(03)00422-8.
Nuriel, P., Weinberger, R., Rosenbaum, G., Golding, S.D., Zhao, J.X., Uysal, I.T., Matthews, M.B., Michael, R.G., 2012. Timing and mechanism of Late-Pleistocene calcite vein formation across the dead sea fault zone, northern Israel. J. Struct. Geol. 36, 43–54. https://doi.org/10.1016/j.jsg.2011.12.010.
Olivarez, A.M., Owen, R.M., 1991. The europium anomaly of seawater: implications for fluvial versus hydrothermal REE inputs to the oceans. Chem. Geol. 92, 317–328. https://doi.org/10.1016/0009-2541(91)90076-4.
Olson, J.E., Laubach, S.E., Lander, R.H., 2009. Natural fracture characterization in tight gas sandstones: integrating mechanics and diagenesis. Am. Assoc. Pet. Geol. Bull. 93, 1535–1549. https://doi.org/10.2118/19007-MS.
Ortega, O.J., Marrett R, A., Laubach, S.E., 2006. A scale-independent approach to fracture intensity and average spacing measurement. Am. Assoc. Pet. Geol. Bull. 90 (2), 193–208. https://doi.org/10.1306/08250505059.
Ougier-Simonin, A., Renard, F., Boehm, C., Vidal-Gilbert, S., 2016. Microfracturing and microporosity in shales. Earth Sci. Rev. 162, 198–226.
Parnell, J., 2010. Potential of palaeofluid analysis for understanding oil charge history. Geofluids 10, 73–78.
Pearson, M.J., Nelson, C.S., 2005. Organic geochemistry and stable isotope composition of New Zealand carbonate concretions and calcite fracture fills. N. Z. J. Geol. Geophys. 48, 395–414. https://doi.org/10.1080/00288306.2005.9515122.
Philippe, M., Manuel, S., 1998. Contrasting origin of palaeofluids in a strike-slip fault system. Chem. Geol. 145, 105–114. https://doi.org/10.1016/S0009-2541(97)00164-2.
Qing, H., Mountjoy, E.W., 1994. Origin of dissolution vugs, caverns, and breccias in the Middle Devonian Presqu'ile barrier, host of Prine Point MVT deposits. Econ. Geol. 89, 858–876. https://doi.org/10.2113/gsecongeo.89.4.858.
Qing, H., Barnes, C.R., Buhl, D., Veizer, J., 1998. The strontium isotopic composition of Ordovician and Silurian brachiopods and conodonts: relationships to geological events and implications for coeval seawater. Geochim. Cosmochim. Acta. 62, 1721–1733. https://doi.org/10.1016/S0016-7037(98)00104-5.
Ren, J.Y., Zhang, J.X., Yang, H.Z., Hu, D.S., 2011. Analysis of fault systems in the central uplift, Tarim Basin. Acta Petrol. Sin. 27, 219–230.
Ren, R., Guan, S.W., Han, B.F., Su, L., 2017. Chronological constraints on the tectonic evolution of the Chinese Tianshan Orogen through detrital zircons from modern and palaeo-river sands. Int. Geol. Rev. 59, 1657–1676.
Robbins, L.J., Lalonde, S.V., Planavsky, N.J., Partin, C.A., Reinhard, C.T., Kendall, B., Scott, C., Hardisty, D.S., Gill, B.C., Alessi, D.S., Dupont, C.L., Saito, M.A., Crowe, S. A., Poulton, S.W., Bekker, A., Lyons, T.W., Konhauser, K.O., 2016. Trace elements at the intersection of marine biological and geochemical evolution. Earth Sci. Rev. 163, 323–348. https://doi.org/10.1016/j.earscirev.2016.10.013.
Roberts, N.M.W., Holdsworth, R.E., 2022. Timescales of faulting through calcite geochronology. A review. J. Struct. Geol. 158, 104578. https://doi.org/10.1016/j.jsg.2022.104578.
Roberts, N.M.W., Rasbury, E.T., Parrish, R.R., Smith, C.J.M., Horstwood, M.S.A., Condon, D.J., 2017. A calcite reference material for LA-ICP-MS U-Pb geochronology. G-cubed 18, 2807–2814. https://doi.org/10.1002/2016GC006784.
Rossi, C., Marfil, R., Ramseyer, K., Permanyer, A., 2001. Facies-related diagenesis and multiphase siderite cementation and dissolution in the reservoir sandstones of the khatatba formation, Egypt's western desert. J. Sediment. Res. 71, 459–472. https://doi.org/10.1306/2DC40955-0E47-11D7-8643000102C1865D.
Sensula, B., Boettger, T., Pazdur, A., Piotrowska, N., Wagner, R., 2006. Carbon and oxygen isotope composition of organic matter and carbonates in recent lacustrine sediments. Geochronometria 25, 77–94. https://doi.org/10.1016/j.geobios.2004.10.004.
Subías, I., Fernández-Nieto, C., 1995. Hydrothermal events in the Valle de Tena (Spanish Western Pyrenees, as evidenced by fluid inclusions and trace-element distribution from fluorite deposits. Chem. Geol. 124, 267–282. https://doi.org/10.1016/0009-2541(95)00060-Y.
Suchy, V., Heijlen, W., Sykorova, I., Muchez, P., Dobes, P., Hladikova, J., Jackova, I., Safanda, Zeman, A., 2000. Geochemical study of calcite veins in the silurian and devonian of the barrandian basin (Czech republic): evidence for widespread Post-Variscan fluid flow in the central part of the bohemian massif. Sediment. Geol. 131, 201–219. https://doi.org/10.1016/S0037-0738(99)00136-0.
Tang, L.J., Huang, T.Z., Qiu, H.J., Wan, G.M., Li, M., Yang, Y., Xie, D.Q., Chen, G., 2014. Fault systems and their mechanisms of the formation and distribution of the Tarim Basin, NW China. J. Earth Sci. 25, 169–182. https://doi.org/10.1111/j.1755-6724.2008.tb00601.x.
Taylor, S.R., Mclennan, S.M., 1985. The continental crust: its composition and evolution. J. Geol. 94, 57–72.
Tong, X.R., Liu, Y.S., Hu, Z.C., Chen, H.H., Zhou, L., Hu, Q.H., Xu, R., Deng, L.X., Chen, C. F., Yang, L., 2016. Accurate determination of Sr isotopic compositions in clinopyroxene and silicate glasses by LA–MC–ICP–MS. Geostand. Geoanal. Res. 40, 85–99.
Ukar, E., Laubach, S.E., 2016. Syn- and postkinematic cement textures in fractured carbonate rocks: insights from advanced cathodoluminescence imaging. Tectonophysics 690 (A), 190–205. https://doi:10.1016/j.tecto.2016.05.001.
Ukar, E., Baqués, V., Laubach, S.E., Marrett, R., 2020. The nature and origins of decameter-scale porosity in Ordovician carbonate rocks, Halahatang oilfield, Tarim Basin, China. J. Geo. Soc. London. 177, 1074–1091. https://doi:10.1144/jgs2019-156.
Uysal, I.T., Golding, S.D., Glikson, M., 2000. Petrographic and isotope constraints on the origin of authigenic carbonate minerals and the associated fluid evolution in Late Permian coal measures, Bowen Basin (Queensland), Australia. Sediment. Geol. 136, 189–206. https://doi.org/10.1016/S0037-0738(00)00097-X.
Veizer, J., Ala, D., Azmy, K., Bruckschen, P., Buhl, D., Bruhn, F., Carden, G.A.F., Diener, A., Ebneth, S., Godderis, Y., Jasper, T., Korte, C., Pawellek, F., Podlaha, O.G., Straus, H., 1999. $^{87}Sr/^{86}Sr$, $\delta^{13}C$ and $\delta^{18}O$ evolution of Phanerozoic seawater. Chem. Geol. 161, 59–88.
Wang, J., Cao, Y.C., Liu, K.Y., Liu, J., Xue, X.J., Xu, Q.S., 2016. Pore fluid evolution, distribution and water-rock interactions of carbonate cements in red-bed sandstone

reservoirs in the Dongying Depression, China. Mar. Pet. Geol. 72, 279–294. https://doi.org/10.1016/j.marpetgeo.2016.02.018.
Wang, J., Cao, Y.C., Liu, K.Y., Costanzo, A., Feely, M., 2018. Diagenesis and evolution of the lower Eocene red-bed sandstone reservoirs in the Dongying Depression, China. Mar. Pet. Geol. 94, 230–245. https://doi.org/10.1016/j.marpetgeo.2018.04.011.
Wang, Z.Y., Gao, Z.Q., Fan, T.L., Shang, Y.X., Qi, L.X., Yun, L., 2020a. Structural characterization and hydrocarbon prediction for the SB5M strike-slip fault zone in the Shuntuo Low Uplift, Tarim Basin. Mar. Pet. Geol. 117, 104418. https://doi.org/10.1016/j.marpetgeo.2020.104418.
Wang, T.F., Jin, Z.K., Shi, Z.W., Dai, X.C., Cheng, R.H., 2020b. Phanerozoic plate history and structural evolution of the Tarim Basin,northwestern China. Int. Geol. Rev. 62, 1555–1569. https://doi.org/10.1080/00206814.2019.1661038.
Wang, J., Pang, Y.H., Cao, Y.C., Peng, J., Liu, K.Y., Liu, H.M., 2021. Sedimentary environment constraints on the diagenetic evolution of clastic reservoirs: examples from the Eocene “red-bed” and “gray-bed” in the Dongying Depression, China. Mar. Pet. Geol. 131, 105153. https://doi.org/10.1016/j.marpetgeo.2021.105153.
Wang, X.T., Wang, J., Cao, Y.C., Han, J., Wu, K.Y., Liu, Y., Liu, K.Y., Xie, M.F., 2022. Characteristics, formation mechanism and evolution model of Ordovician carbonate fault-controlled reservoirs in the Shunnan area of the Shuntuoguole lower uplift, Tarim Basin, China. Mar. Pet. Geol. 145, 105878. https://doi.org/10.1016/j.marpetgeo.2022.105878.
Wang, S., Liu, K., Wang, J., Li, Y., Li, Z., Yang, H., Mo, T., 2023. Geochemistry of syntaxial calcite veins in ultra-deep sandstone reservoirs from the Kuqa depression, western China. J. Struct. Geol. 173, 104895. https://doi.org/10.1016/j.jsg.2023.104895.
Wang, J., Wang, X.T., Cao, Y.C., Hao, F., Pang, Y.H., Yun, L., Yang, H.J., Xie, M.F., 2024. Characteristics and origin of the ultradeep Ordovician fault-karst reservoirs: an example from the Shunbei-Yuejin area, Tarim Basin. Am. Assoc. Pet. Geol. Bull. 108, 1231–1260. https://doi.org/10.1306/10052321152.
Watkins, J.M., Hunt, J.D., Ryerson, F.J., DePaolo, D.J., 2014. The influence of temperature, pH, and growth rate on the δ18O composition of inorganically precipitated calcite. Earth Planet Sci. Lett. 404, 332–343. https://doi.org/10.1016/j.epsl.2014.07.036.
Watkins, H., Bond, C.E., Cawood, A.J., Cooper, M.A., Warren, M.J., 2020. Fracture distribution on the swift reservoir anticline Montana: implications for structural and lithological controls on fracture intensity. Geol. Soc. Lond. Spec. Publ. 487, 209–228. https://doi.org/10.1144/SP487.9.
Webb, G.E., Nothdurft, L.D., Kamber, B.S., Kloprogge, J.T., Zhao, J.X., 2008. Rare earth element geochemistry of scleractinian coral skeleton during meteoric diagenesis: a sequence through neomorphism of aragonite to calcite. Sedimentology 56, 1433–1463. https://doi.org/10.1111/j.1365-3091.2008.01041.x.
Worden, R.H., Benshatwan, M.S., Potts, G.J., Elgarmadi, S.M., 2016. Basin-scale fluid movement patterns revealed by veins: wessex Basin, UK. Geofluids 16, 149–174. https://doi.org/10.1111/gfl.12141.
Wu, M.B., Wang, Y., Zheng, M.L., Zhang, W.B., Liu, C.Y., 2007. The hydrothermal karstification and its effect on Ordovician carbonate reservoir in Tazhong uplift of Tarim Basin, Northwest China. Sci. China Earth Sci. 50, 103–113. https://doi.org/10.1007/s11430-007-6026-x.
Wu, N., Cai, Z.X., Yang, H.J., Wang, Z.Q., Liu, X.F., Han, J.F., 2013. Hydrocarbon charging of the Ordovician reservoirs in Tahe-Lunnan area, China. Sci. China Earth Sci. 56, 763–772. https://doi.org/10.1007/s11430-013-4598-1.
Wu, G.H., Gao, L.H., Zhang, Y.T., Ning, C.Z., Xie, E., 2018. Fracture attributes in reservoir-scale carbonate fault damage zones and implications for damage zone width and growth in the deep subsurface. J. Struct. Geol. 118, 181–193. https://doi.org/10.1016/j.jsg.2018.10.008.
Wu, G.H., Kim, Y.S., Su, Z., Yang, P.F., Ma, D.B., Zheng, D.M., 2020a. Segment interaction and linkage evolution in a conjugate strike-slip fault system from the Tarim Basin, NW China. Mar. Pet. Geol. 112, 104054. https://doi.org/10.1016/j.marpetgeo.2019.104054.
Wu, G.H., Zhao, K.Z., Qu, H.Z., Scarselli, N., Zhang, Y.T., Han, J.F., Xu, Y.F., 2020b. Permeability distribution and scaling in multi-stages carbonate damage zones: insight from strike-slip fault zones in the Tarim Basin, NW China. Mar. Pet. Geol. 114, 104–208. https://doi.org/10.1016/j.marpetgeo.2019.104208.
Wu, G.H., Ma, B.S., Han, J.F., Guan, B.Z., Chen, X., Yang, P., Xie, Z., 2021. Origin and growth mechanisms of strike-slip faults in the central Tarim cratonic basin, NW China. Pet. Explor 48, 595–607. https://doi.org/10.1016/S1876-3804(21)60048-4.
Xu, Z.Q., Li, S.T., Zhang, J.X., Yang, J.S., He, B.Z., Li, H.B., Lin, C.S., Cai, Z.H., 2011. Paleo-asian and tethyan tectonic systems with docking the Tarim block. Acta Petrol. Sin. 27, 1–22. https://doi.org/10.1134/S002449021101007X.
Yang, P., Liu, K.Y., Liu, J.L., Yang, S., Yu, B., Hou, M.g., Wu, L.Y., 2021. Petroleum charge history of deeply buried carbonate reservoirs in the Shuntuoguole Low Uplift, Tarim Basin, west China. Mar. Pet. Geol. 128, 105063. https://doi.org/10.1016/j.marpetgeo.2021.105063.
Yang, P., Liu, K.Y., Li, Z., Rankenburg, K., McInnes, B.I.A., Liu, J.L., Evans, N.J., 2022a. Direct dating Paleo-fluid flow events in sedimentary basins. Chem. Geol. 588, 120642. https://doi.org/10.1016/j.chemgeo.2021.120642.
Yang, L., Yu, L., Liu, K.Y., Jia, J.H., Zhu, G., Liu, Q., 2022b. Coupled effects of temperature and solution compositions on metasomatic dolomitization: significance and implication for the formation mechanism of carbonate reservoir. J. Hydrol. 604, 127199. https://doi.org/10.1016/j.jhydrol.2021.127199.
Yuan, C., Sun, M., Zhou, M.F., Zhou, H., Xiao, W.J., Li, J.L., 2002. Tectonic evolution of the West Kunlun: geochronologic and geochemical constraints from kudi granitoids. Int. Geol. Rev. 44, 653–669. https://doi.org/10.2747/0020-6814.44.7.653.
Zeng, L., Li, X.Y., 2009. Fractures in sandstone reservoirs with ultralow permeability: a case study of the upper triassic yanchang formation in the ordos basin, China. Am. Assoc. Pet. Geol. Bull. 93, 461–477. https://doi.org/10.1306/09240808047.
Zhang, C.L., Zou, H.B., Li, H.L., Wang, H.Y., 2013. Tectonic framework and evolution of the Tarim block in NW China. Gondwana Res. 23, 1306–1315. https://doi.org/10.1016/j.gr.2012.05.009.
Zhang, Z.Y., Zhu, W.B., Zheng, D.W., Zheng, B.H., Xiao, W.J., Li, D.M., Han, C.M., 2017. Neoproterozoic-paleozoic tectonic evolution of the northeastern Tarim block: constraints from 40Ar/39Ar geochronology in the kuluketage area, NW China. Acta Geol. Sin.-Engl. 91, 1231–1247. https://doi.org/10.3969/j.issn.1000-9515.2017.04.006.
Zhang, C.L., Zou, H.B., Ye, X.T., Chen, X.Y., 2018. Timing of subduction initiation in the proto-tethys ocean: evidence from the cambrian gabbros from the NE pamir plateau. Lithos 314–315, 40–51. https://doi.org/10.1016/j.lithos.2018.05.021.
Zhang, Q.C., Wu, Z.H., Chen, X.H., Zhou, Q., Shen, N.P., 2019. Proto-tethys oceanic slab break-off: insights from early paleozoic magmatic diversity in the West Kunlun orogen, NW Tibetan plateau. Lithos 346–347, 105147. https://doi.org/10.1016/j.lithos.2019.07.014.
Zhao, R., Zhao, T., Kong, Q.F., Deng, S., Li, H.L., 2020. Relationship between fractures, stress, strike-slip fault and reservoir productivity, China Shunbei oil field, Tarim Basin. Carbonates Evaporites 35, 84. https://doi.org/10.1007/s13146-020-00612-6.